



# OPEN Synthesis and characterization of hematite nanomaterials imprinted with acetone, ethanol and methanol for AI-Based IoT gas sensor arrays

Rana M. Abdelghani<sup>1,2</sup>, Abd El-Hady B. Kashyout<sup>3</sup>, Iman Morsi<sup>4</sup>, Taha Elsayed Taha<sup>1</sup>, Naglaa F. Soliman<sup>5</sup> & Walid El-Shafai<sup>1,6</sup>✉

Indoor air pollution, primarily caused by volatile organic compounds (VOCs) such as acetone, ethanol, and methanol, poses significant health risks and necessitates the development of efficient, real-time monitoring solutions. Conventional gas sensors often operate at high temperatures and are limited to detecting a single gas type, which restricts their applicability for comprehensive air quality management. To address these challenges, this study presents the development and evaluation of an advanced electronic nose (E-nose) system capable of detecting acetone, ethanol, and methanol at low operating temperatures. The proposed E-nose system comprises a gas sensor array integrating three metal oxide sensors (SM10, SE10, and Sp) designed for the simultaneous detection of these VOCs. The sensor array is seamlessly combined with Internet of Things (IoT) and cloud-based platforms to enable real-time gas monitoring and analysis. Hematite nanomaterials, imprinted with ethanol and methanol at varying concentrations of 10%, 15%, and 25%, were synthesized via a hydrothermal method. Comprehensive characterization of the synthesized nanopowders was performed using scanning electron microscopy (SEM), X-ray diffraction (XRD), photoluminescence (PL), and thermogravimetric analysis (TGA). Electrical performance assessments, including response versus temperature, resistance versus gas concentration, and output voltage versus gas concentration, were conducted to evaluate sensor efficiency. To enhance the accuracy and reliability of gas detection, artificial intelligence (AI) algorithms were employed to analyze sensor data, enabling precise gas concentration monitoring and issuing alerts when predefined threshold levels are exceeded. The dataset, obtained from sensor responses to different concentrations of acetone, ethanol, and methanol, was analyzed using multiple hybrid machine learning models, including CNN-LSTM, PCA-CNN-LSTM, PCA-XGBoost, Random Forest (RF), RF-GB, RF-GB-NN, and KNN. Notably, the RF, RF-GB, and RF-GB-NN models achieved 100% accuracy in classifying both gas type and condition. Regression analysis further demonstrated that the RF-GB model achieved an ideal coefficient of determination ( $R^2 = 1$ ) across all three gases, with RF and RF-GB-NN yielding  $R^2$  values of 0.999. Among the models, RF-GB exhibited the lowest limit of detection (LOD), while RF presented relatively higher LOD values. The findings validate the effectiveness of the developed sensor array, combined with AI-driven analysis, in accurately classifying and quantifying gas concentrations. Threshold values were established at 500 ppm for acetone and ethanol, and 200 ppm for methanol, with monitoring capabilities tailored to these limits.

**Keywords** Hematite nanomaterials, Ethanol imprinting, Methanol imprinting, IoT, Gas sensor array, AI algorithms, Solid state sensors

<sup>1</sup>Department of Electronics and Electrical Communications Engineering, Faculty of Electronic Engineering, Menoufia University, Menouf 32952, Egypt. <sup>2</sup>Alexandria Higher Institute of Engineering and Technology, Alexandria 21615, Egypt. <sup>3</sup>Electronic Materials Research Department, Advanced Technology and New Materials Research Institute, City of Scientific Research and Technological Applications (SRTA-City), New Borg El-Arab City, Alexandria 21934, Egypt. <sup>4</sup>Arab Academy for Science and Technology, and Maritime Transport, Alexandria 1029, Egypt. <sup>5</sup>Department of Information Technology, College of Computer and Information Sciences, Princess Nourah bint Abdulrahman University, P.O. Box 84428, 11671 Riyadh, Saudi Arabia. <sup>6</sup>Automated Systems and Computing Lab (ASCL), Prince

Sultan University, 11586 Riyadh, Saudi Arabia. ✉email: walid.elshafai@el-eng.menofia.edu.eg; welshafai@psu.edu.sa; eng.waled.elshafai@gmail.com

The integration of artificial intelligence (AI) in environmental monitoring and health management has significantly advanced in recent years<sup>1–3</sup>. The application of AI technologies for indoor air quality assessment has become increasingly crucial due to rising concerns about air pollution and its adverse effects on human health<sup>4–7</sup>. Among the various AI-driven solutions, electronic nose (E-nose) systems have emerged as a pivotal application, leveraging machine learning algorithms to effectively monitor and manage indoor air quality<sup>8,9</sup>. These systems provide real-time detection and analysis of airborne pollutants, offering a robust approach to ensuring healthier indoor environments.

In recent years, the significance of clean air has been increasingly recognized, as indoor air pollution poses a critical threat to human health, contributing to a substantial number of fatalities annually<sup>10</sup>. Volatile organic compounds (VOCs), including methanol, benzene, formaldehyde, acetone, and ammonia, are among the primary contributors to indoor air pollution<sup>11–13</sup>. Exposure to elevated concentrations of acetone, in particular, can have detrimental effects on vital organs, potentially leading to severe health complications<sup>14,15</sup>.

Metal oxide semiconductors have been extensively utilized for gas sensing applications due to their high efficiency and cost-effectiveness<sup>16</sup>. Various metal oxides, including SnO<sub>2</sub>, TiO<sub>2</sub>, ZnO, In<sub>2</sub>O<sub>3</sub>, Fe<sub>2</sub>O<sub>3</sub>, and WO<sub>3</sub>, have been widely investigated for their superior gas sensing capabilities<sup>17,18</sup>. Among these materials, iron oxide (Fe<sub>2</sub>O<sub>3</sub>) stands out as a preferred choice due to its remarkable stability, non-toxicity, and high efficiency in detecting a wide range of gases<sup>19</sup>. Recent advancements in Fe<sub>2</sub>O<sub>3</sub> nanomaterials have focused on the development of diverse morphologies to enhance sensor performance and sensitivity<sup>20</sup>.

Molecular Imprinting Technology (MIT) has gained significant attention as an effective approach for gas detection, leveraging its ability to create molecularly imprinted polymers (MIPs) with precisely tailored cavities that exhibit high selectivity for target gases<sup>21</sup>. MIT can be categorized into three primary techniques: bulk imprinting, surface imprinting, and epitope imprinting, each offering distinct advantages and design flexibility for sensor development<sup>21</sup>. These techniques enable the fabrication of highly sensitive and selective gas sensors, enhancing their potential for diverse environmental monitoring applications.

Ensuring high indoor air quality is crucial, particularly in modern homes equipped with advanced Internet of Things (IoT) systems that facilitate real-time monitoring and control<sup>22</sup>. VOCs such as methanol, ethanol, and acetone, commonly found in industrial and domestic products, pose significant health risks and negatively impact indoor air quality<sup>11</sup>. Acetone, widely used in household products such as nail polish removers and cleaning agents, can have severe effects on the central nervous system and vital organs when its concentration exceeds 173 ppm. Consequently, a safety threshold of 500 ppm has been established for acetone exposure<sup>23,24</sup>. Prolonged exposure to acetone can also cause irritation to the eyes and respiratory system<sup>23</sup>.

Ethanol, frequently used in alcohol-based products and sanitizers, has a recommended safe exposure limit of 500 ppm; however, concentrations exceeding 1000 ppm can cause skin irritation, while levels above 3300 ppm may lead to central nervous system depression<sup>25</sup>. Similarly, methanol, commonly present in industrial products and fuels, presents a higher risk, with a safe exposure limit of 200 ppm. Exposure beyond this threshold can result in adverse health effects, including headaches, nausea, dizziness, and blurred vision. Extremely high methanol concentrations (exceeding 6000 ppm) can lead to severe metabolic acidosis, blindness, and even fatal outcomes<sup>26</sup>.

The integration of electronic nose (E-nose) technology in smart home systems represents an innovative solution for real-time air quality monitoring and management, offering a proactive approach to mitigating the risks associated with VOC exposure.

## Research problem

Indoor air pollution has emerged as a pressing global concern, with VOCs such as acetone, ethanol, and methanol contributing significantly to air quality deterioration. Prolonged exposure to these pollutants can lead to severe health issues, including respiratory problems, neurological disorders, and organ damage. Conventional gas sensors, although widely used, often suffer from limitations such as high operating temperatures, selectivity issues, and limited real-time monitoring capabilities. These challenges underscore the need for advanced sensing solutions that offer high sensitivity, selectivity, and rapid response times.

## Research motivation

The motivation for this research stems from the growing demand for real-time, cost-effective, and highly sensitive gas monitoring systems that can be seamlessly integrated into smart home and industrial environments. The emergence of IoT technologies and AI-driven analytics presents a promising opportunity to enhance gas sensing capabilities. By leveraging IoT-enabled gas sensor arrays combined with AI algorithms, this study aims to overcome the limitations of traditional sensing methods and provide a more efficient and intelligent solution for air quality management.

## Research contribution

This study introduces an innovative AI-enhanced electronic nose (E-nose) system, uniquely integrating metal oxide gas sensors with IoT technologies for real-time detection and monitoring of VOCs, specifically acetone, ethanol, and methanol. A notable novelty of this research is the first-ever employment of molecular imprinting techniques using ethanol, methanol, and acetone at varying concentrations (10%, 15%, and 25%) to synthesize hematite nanomaterials via a hydrothermal method. This approach yields cost-effective sensors with tailored selectivity and significantly improved sensitivity, effectively addressing the high-temperature operational

limitations typically encountered by conventional gas sensors. Notably, the designed sensor array operates efficiently at considerably lower temperatures.

An additional novel contribution involves the utilization of advanced hybrid artificial intelligence and machine learning methodologies, including CNN-LSTM, Principal Component Analysis-CNN-LSTM (PCA-CNN-LSTM), PCS-eXtreme Gradient Boosting (PCA-XGBoost), Random Forest (RF), Random Forest-Gradient Boosting (RF-GB), RF-GB-Neural Network (RF-GB-NN), and K-Nearest Neighbors (KNN). This comprehensive and innovative hybrid modeling approach, applied collectively for the first time in this context, demonstrated exceptional performance in gas classification and concentration prediction tasks, achieving up to 100% classification accuracy and near-perfect regression outcomes.

Moreover, this study uniquely investigates the electrical characteristics of these sensor devices in diode configurations through rigorous current–voltage (I–V) characterization for the first time. Both linear (ohmic) and rectifying (diode-like) behaviors were systematically identified across various molecularly imprinted samples. This exploration provides essential insights into charge transport mechanisms, conductivity variations, and rectification characteristics—parameters critical to the sensors' performance optimization in practical gas sensing and IoT implementations.

The synthesized nanomaterials underwent comprehensive characterization employing advanced analytical techniques such as scanning electron microscopy (SEM), X-ray diffraction (XRD), photoluminescence (PL), and thermogravimetric analysis (TGA). These methods elucidated the structure–performance relationships crucial for sensor efficiency. Furthermore, the system's electrical performance was thoroughly evaluated by examining response characteristics versus temperature, resistance as a function of gas concentration, and output voltage relative to gas concentration, confirming robust reliability and operational efficiency at reduced temperatures.

Collectively, these integrated innovations, including pioneering diode characterization, establish a novel standard in intelligent gas sensor technology, providing practical, scalable solutions suitable for smart home systems, industrial monitoring, and healthcare diagnostics.

The structure of this paper is organized as follows. First, the experimental procedures for the synthesis of nanopowders and the fabrication of the E-nose device are described. Next, a comprehensive characterization of the nanopowder morphology and physicochemical properties using various analytical techniques is presented. Following this, the electrical properties of the sensor array are analyzed, providing insights into its performance under different operating conditions. Subsequently, the implementation of AI models for gas detection and analysis is detailed, emphasizing the methodologies used and their effectiveness. Finally, an in-depth discussion of the findings and their implications is provided, culminating in the conclusion.

## Proposed methodology

This section outlines the methodological approach adopted to develop an AI-enhanced E-nose system for detecting VOCs, specifically acetone, ethanol, and methanol. The proposed methodology consists of two main phases: experimental and simulation. The experimental phase focuses on the synthesis and characterization of hematite ( $\text{Fe}_2\text{O}_3$ ) nanomaterials, the fabrication of the gas sensor array, and the collection of sensor response data under controlled conditions. The simulation phase leverages the collected dataset to optimize the E-nose system through data preprocessing, feature extraction, and the application of advanced machine learning algorithms to classify gas types and conditions. The following subsections provide detailed insights into the experimental procedures, characterization techniques, data collection, and AI-based simulation strategies employed to achieve efficient and accurate gas detection.

## Proposed experimental work

This study aims to develop a cost-effective and efficient electronic nose (E-nose) system capable of detecting VOCs, specifically acetone, ethanol, and methanol, at low operating temperatures. The primary objective is to enable real-time monitoring of gas type and condition, facilitating practical applications such as indoor air quality management.

### *Fabrication of gas sensor array*

To develop an economical and efficient gas sensor array, hematite ( $\text{Fe}_2\text{O}_3$ ) nanomaterials were synthesized using the hydrothermal method. MIT was employed as a straightforward and preparation-oriented approach to enhance the sensing capabilities of nanomaterials. The imprinting process was designed to impart selective efficiency to the hematite nanomaterials, enabling them to detect ethanol, methanol, and acetone by imprinting them with their respective target gases. Various imprinting ratios of ethanol and methanol (10%, 15%, and 25%) were explored to optimize the gas response. The resulting sensor devices were tailored to achieve high sensitivity and reliable detection at low operating temperatures, offering a cost-effective alternative to conventional E-nose systems that typically rely on expensive sensor technologies.

### *Characterization of synthesized materials*

The synthesized hematite nanomaterials underwent comprehensive characterization using advanced analytical techniques to assess their physical, chemical, and optical properties. SEM was employed to analyze morphology and particle size, while XRD was utilized to confirm the crystalline structure of the materials. PL spectroscopy was performed to investigate optical properties, and Thermogravimetric Analysis TGA was conducted to evaluate thermal stability and the presence of residual components. These characterization techniques provided critical insights into the material properties, facilitating further optimization of the sensor performance.

### Measurements and dataset collection

The fabricated sensor devices underwent a series of electrical performance tests to assess their efficiency in detecting VOCs. These tests included evaluating the sensor response across different temperature ranges to determine optimal operating conditions, measuring resistance changes to assess sensor sensitivity, and analyzing output voltage variations with respect to gas concentrations. The collected data, particularly the relationship between output voltage and gas concentration, was compiled into a comprehensive dataset capturing sensor responses to acetone, ethanol, and methanol at varying concentrations. Threshold concentrations for real-time monitoring were established at 500 ppm for acetone and ethanol, and 200 ppm for methanol. This dataset formed a crucial basis for the subsequent simulation phase, enabling the application of machine learning algorithms to accurately classify gas types and conditions, ensuring precise and reliable monitoring capabilities.

### Proposed simulation work

The simulation phase focuses on utilizing the experimental dataset to optimize the performance of the E-nose system, with an emphasis on real-time monitoring of gas types and conditions for practical end-user applications.

### Data preprocessing and analysis

The raw data collected from sensor responses included measurements of output voltage as a function of gas concentration for acetone, ethanol, and methanol across a range of concentrations. Additionally, variations in sensor responses under different environmental conditions were recorded, providing a comprehensive dataset for analysis. To ensure accuracy and consistency, the data underwent preprocessing steps such as normalization, which scaled the data within a uniform range, and feature extraction to identify the most relevant patterns and trends. These preprocessing techniques were critical in preparing the data for effective training and evaluation of AI models, facilitating precise classification of gas types and conditions.

### Application for AI models

A total of seven machine learning models were employed to classify gas types and conditions, as well as to predict gas concentrations. The models included Convolutional Neural Network-Long Short-Term Memory (CNN-LSTM), Principal Component Analysis-CNN-LSTM (PCA-CNN-LSTM), PCA-XGBoost, Random Forest (RF), Random Forest and Gradient Boosting (RF-GB), RF-GB with Neural Networks (RF-GB-NN), and K-Nearest Neighbors (KNN). These models were evaluated based on their accuracy, reliability, and efficiency in gas concentration monitoring. The primary objective of this evaluation was to identify the most suitable models for accurate classification of gas types and conditions while ensuring timely alerts when predefined threshold levels were exceeded.

## Experimental section

### Fabrication of metal oxide gas sensor array

#### Synthesis of imprinted nano-hematite

Hematite ( $\text{Fe}_2\text{O}_3$ ) nanomaterials were synthesized using a hydrothermal method, following a similar approach to our previous work on acetone imprinting<sup>27</sup>. The novelty of this study lies in the utilization of ethanol and methanol as imprinting agents in varying ratios (10%, 15%, and 25%) to investigate their impact on the structural, morphological, and gas-sensing properties of hematite nanomaterials. The incorporation of AI algorithms further enhances the study by enabling precise gas concentration monitoring through sensor response data analysis. This AI integration provides accurate quantification of gas concentrations and offers deeper insights into the relationship between imprinting conditions and gas-sensing performance, representing a substantial advancement over previous studies.

**Ethanol and methanol imprinting** The fabrication of hematite nanomaterials in this study utilized ethanol and methanol as imprinting agents, with concentrations of 10%, 15%, and 25% based on the volume of the imprinting agent relative to the total solution volume. These ratios were selected to explore the optimal balance between effective gas molecule adsorption and the structural integrity of the imprinted material. We hypothesized that increasing the concentration of the imprinting agent would enhance the adsorption capacity by providing more surface area for gas molecules<sup>28</sup>. However, higher ratios could potentially compromise the structural stability and adsorption efficiency due to overcrowding or unfavorable interactions within the matrix.

The synthesis process began by dissolving iron chloride ( $\text{FeCl}_3 \cdot 6\text{H}_2\text{O}$ , 3.24 g) and 0.5 ml of hydrochloric acid (HCl, 38%) in deionized water. Ethanol or methanol was then added at the specified volumes, 10 ml for the 10% ratio, 15 ml for the 15% ratio, and 25 ml for the 25% ratio, while the total solution volume was adjusted to 100 ml. Ammonium hydroxide ( $\text{NH}_4\text{OH}$ ) was introduced dropwise to raise the pH to 11, followed by two hours of stirring at room temperature. The mixtures were then transferred to Teflon-lined stainless-steel autoclaves for hydrothermal treatment at 130 °C for 90 min.

After hydrothermal treatment, the products were washed three times with ethanol or methanol, centrifuged, and dried in a vacuum furnace at 80 °C for 20 h. This process resulted in six  $\alpha\text{-Fe}_2\text{O}_3$  nanopowder samples, labeled according to the imprinting agent and ratio: E10, E15, and E25 for ethanol, and M10, M15, and M25 for methanol.

The imprinting process was designed to ensure selective adsorption properties, with imprinting agents being used both during the synthesis and the washing stages. The inclusion of ethanol and methanol as imprinting agents is aimed at optimizing the sensor's ability to interact with specific gases, thereby enhancing sensor performance for gas detection. The ratios were chosen to explore how varying the imprinting agent concentration impacts the material's surface area and adsorption efficiency, which ultimately influences the sensor's gas response.

## Sensor device fabrication and gas sensing measurement

### *Sensor device fabrication*

To fabricate the solid-state gas sensors, 1 mg of the synthesized  $\alpha$ -Fe<sub>2</sub>O<sub>3</sub> nanopowders (E10, E15, E25, M10, M15, and M25) was mixed with 2 mg of ethanol and stirred continuously for seven days<sup>6</sup>. The resulting homogeneous solution was applied onto a pre-cleaned and sanded glass substrate using a wafer spinner machine (Model: Polos 300 AWS) set at 600 rpm for 2 min to achieve the desired film thickness. The prepared thin films were then left to air dry to ensure uniformity. To enhance adhesion, the glass substrate was sanded using fine-grit sandpaper prior to coating. Platinum (Pt) contact electrodes were deposited onto each of the six prepared films using a sputtering device (Photon Coating System Model: PH-260sv), operating at 100 W RF power for 5 min. This process ensured the formation of reliable electrical contacts for gas sensing applications.

### *Gas sensing measurements*

Gas sensing experiments were conducted to evaluate the electrical resistance variations of the thin films in response to different VOC concentrations at controlled operating temperatures. Ethanol and methanol gases were introduced into a custom-designed gas chamber with dimensions of 20 cm × 20 cm × 20 cm. The sensor response was measured by monitoring resistivity changes as a function of gas temperature, ranging from 30 to 300 °C, to determine the optimal operating temperature. The fabricated sensors had dimensions of 2 cm × 2 cm. The gas response, denoted by “S,” is calculated using the following equation<sup>21</sup>:

$$S = (R_a/R_g) \times 100 \quad (1)$$

where  $R_a$  represents the resistance of the sensor in air, and  $R_g$  represents the resistance in the presence of the target gas.

Temperature during gas sensing experiments was controlled using a built-in heater equipped with a thermocouple device. The heater was calibrated to ensure that the gas temperature matched the heater temperature once the chamber was fully wrapped and thermally stabilized. The gas temperature was systematically varied from 30 to 300 °C, and the optimal sensing temperature was determined based on the maximum gas response. Gas-sensing measurements were conducted under controlled absolute humidity conditions, maintaining a level between 40 and 60 g/m<sup>3</sup>, which was continuously monitored to ensure consistent environmental stability.

To control the gas concentration, a predetermined volume of pure liquid acetone was injected into a homemade sealed gas chamber (20 cm × 20 cm × 20 cm)<sup>27</sup>. The complete evaporation of the injected liquid enabled accurate calculation of the gas-phase concentration using the following formula:

$$\frac{22.4\rho TV_s}{273MV} \times 1000 \quad (2)$$

where  $\rho$  is the density of ethanol and methanol, 0.789 g/cm<sup>3</sup> and 0.7918 g/cm<sup>3</sup>, respectively, T is the temperature in Kelvin,  $V_s$  is the injected volume in  $\mu$ L, M is the molar mass of acetone (58.08 g/mol), and V is the chamber volume in m<sup>3</sup>. This method assumes complete evaporation of the ethanol and methanol.

Since the system operates based on static evaporation within a sealed chamber, homogeneous gas distribution was achieved by allowing sufficient diffusion time after injection. After each measurement, the chamber was ventilated by manually purging with clean air to remove residual gases and reestablish baseline conditions.

Each gas-sensing measurement at a given concentration was repeated three times on different days to assess repeatability, with consistent responses observed across all trials. Furthermore, long-term stability tests were conducted over a period of 30 days, during which the sensor response was measured at regular five-day intervals under the same testing conditions, demonstrating reliable and stable sensor performance over time.

The gas sensing mechanism of the metal oxide semiconductor (MOS) sensors is based on the interaction between the gas molecules and the sensor surface, leading to changes in the electrical properties. When gas molecules adsorb onto the metal oxide surface, an electrically polarized layer forms at the metal–insulator/oxide interface, resulting in a decrease in the sensor’s barrier height. Consequently, the reduction in the electric field at the metal–insulator boundary leads to a voltage drop due to the decreased metal–semiconductor work function<sup>29</sup>.

To analyze the electrical characteristics of the fabricated sensors, a METROHM Autolab 87,070 Potentiostat was used to perform current–voltage (I–V) measurements by applying a voltage range from –5 V to +5 V. The analysis included evaluating the dark current, series resistance, shunt resistance, and rectifying ratio for the SM10 sample, while only resistance measurements were conducted for the linear I–V characteristics of the SE10, SE15, SE25, SM15, and SM25 devices (Check Table 1).

## Characterization of gas-sensing nanopowder properties

The synthesized  $\alpha$ -Fe<sub>2</sub>O<sub>3</sub> nanopowders were characterized using a range of advanced analytical techniques to evaluate their structural, morphological, elemental, optical, and thermal properties. XRD analysis was conducted using a Shimadzu 6000 diffractometer at a scan rate of 8° per minute for 2 $\theta$ , utilizing Cu K $\alpha$  radiation ( $\lambda$  = 0.15406 nm) generated at an operating voltage of 40 kV and a current of 30 mA. The diffraction patterns were recorded over a Bragg angle ( $\theta$ ) range of 5° to 80° to determine the crystallographic structure and phase composition of the synthesized powders<sup>30</sup>.

The morphological characteristics of the synthesized materials, including particle size and surface texture, were analyzed using Field Emission Scanning Electron Microscopy (FESEM) with a JSM-IT200 series instrument. Additionally, elemental composition analysis was performed using an integrated Energy-Dispersive X-ray Spectroscopy (EDX) system to confirm the presence and distribution of elements in the samples.



Sensor symbol	Film symbol	Imprinting material	Imprinting ratio	Washing solution
SE10	E10	Ethanol	10%	Ethanol
SE15	E15	Ethanol	15%	Ethanol
SE25	E25	Ethanol	25%	Ethanol
SM10	M10	Methanol	10%	Methanol
SM15	M15	Methanol	15%	Methanol
SM25	M25	Methanol	25%	Methanol
Spure	Pure	–	–	Water

**Table 1.** Conditions for the fabrication of sensor films.

PL measurements were carried out to assess the optical properties of the synthesized nanomaterials. A He-Cd laser (Kimmon—325 nm) was employed as the excitation source, and the spectra were recorded using a Synapse CCD camera connected to an iHR320 spectrometer (HORIBA), covering a wavelength range from 300 to 900 nm<sup>31</sup>.

The thermal stability of the imprinted iron oxide nanomaterials at various imprinting percentages was evaluated using a thermogravimetric analyzer (Shimadzu TGA-50 H, Japan). The TGA provided insights into the thermal decomposition behavior and weight loss characteristics of the samples, aiding in the determination of their thermal resilience under different conditions<sup>32</sup>.

Fourier Transform Infrared (FTIR) spectroscopy was performed to identify the functional groups present in the synthesized nanomaterials. The FTIR spectra were recorded using a Shimadzu 8400S spectrometer (Japan), with a transmission range spanning from 4000 to 400 cm<sup>-1</sup>, providing valuable information on the chemical bonding and molecular structure of the samples.

## Results and discussion

### Characterization of nanopowders

A comprehensive analysis of the characterization results is presented for each imprinting ratio, providing a comparative evaluation of ethanol- and methanol-imprinted nanomaterials.

#### Scanning electron microscopy (SEM) analyses

The SEM images in Fig. 1 illustrate significant variations in particle size, morphology, and structural arrangement among the ethanol- and methanol-imprinted samples. For the ethanol-imprinted nanomaterials, the E10 sample exhibits the largest particle size, with distinct morphological features and an average diameter of 0.099  $\mu\text{m}$ . As the ethanol concentration increases in the E15 sample, the particles tend to agglomerate, forming clusters with an average size of 0.075  $\mu\text{m}$ . At an ethanol imprinting ratio of 25% (E25), the nanoparticles become more condensed, displaying smoother surfaces and cubic-like structures, with an average particle size of 0.0894  $\mu\text{m}$ . These findings suggest that higher ethanol concentrations contribute to a more compact and uniform particle structure, likely influencing the material's gas-sensing properties.

In contrast, the methanol-imprinted samples exhibit distinct morphological characteristics. The M10 sample features finer, dust-like particles with an average size of 0.118  $\mu\text{m}$ , indicating a different crystallization and growth dynamic compared to ethanol-imprinted samples. This variation in particle formation suggests that the methanol imprinting process influences the structural evolution of hematite nanomaterials differently than ethanol, potentially impacting their gas adsorption behavior and sensing performance.

The histogram in Fig. 2 presents a quantitative analysis of the particle size distribution and standard deviation (SD) for the four samples (E10, E15, E25, and M10). Among the ethanol-imprinted samples, E10 exhibits the largest average particle size (0.099  $\mu\text{m}$ , SD: 0.0281  $\mu\text{m}$ ) and demonstrates the highest gas response. This suggests that larger particles facilitate more effective gas diffusion and interaction with the sensor surface, enhancing adsorption efficiency and overall sensor sensitivity<sup>27</sup>.

In contrast, the E15 (0.075  $\mu\text{m}$ , SD: 0.019  $\mu\text{m}$ ) and E25 (0.0894  $\mu\text{m}$ , SD: 0.0194  $\mu\text{m}$ ) samples consist of smaller particles forming more compact structures, which may restrict gas diffusion and reduce sensing efficiency. Meanwhile, the methanol-imprinted M10 sample, characterized by finer particles (0.118  $\mu\text{m}$ , SD: 0.0235  $\mu\text{m}$ ), offers an increased surface area, potentially enhancing sensitivity by providing additional adsorption sites for gas molecules. These findings highlight the critical role of particle size in determining the gas-sensing performance of the materials, where an optimal balance between particle size and surface area is crucial for maximizing sensor efficiency.

The Energy-Dispersive X-ray Spectroscopy (EDX) results, presented in Fig. 3, further emphasize the elemental composition differences among the samples. For the E10 sample, the elements C, O, and Fe are present at weight percentages of 7.81%, 24.16%, and 4.59%, respectively, with corresponding atomic percentages of 18.99%, 44.08%, and 3.78%. In the E15 sample, the weight percentages of C, O, and Fe are 6.74%, 29.26%, and 63.99%, while their atomic percentages are 15.88%, 51.72%, and 32.4%, respectively. Similarly, for the E25 sample, the weight percentages are 21.72%, 27.07%, and 51.21%, with atomic percentages of 40.93%, 38.31%, and 20.76%, respectively.

Figure 4 illustrates the EDX results for both the pure sample and the M10 sample. The pure sample contains C, O, and Fe at weight percentages of 10.05%, 34.93%, and 55.02%, with atomic percentages of 20.89%, 54.51%, and 24.6%, respectively. The M10 sample exhibits weight percentages of 20.44%, 33.72%, and 45.83%, corresponding

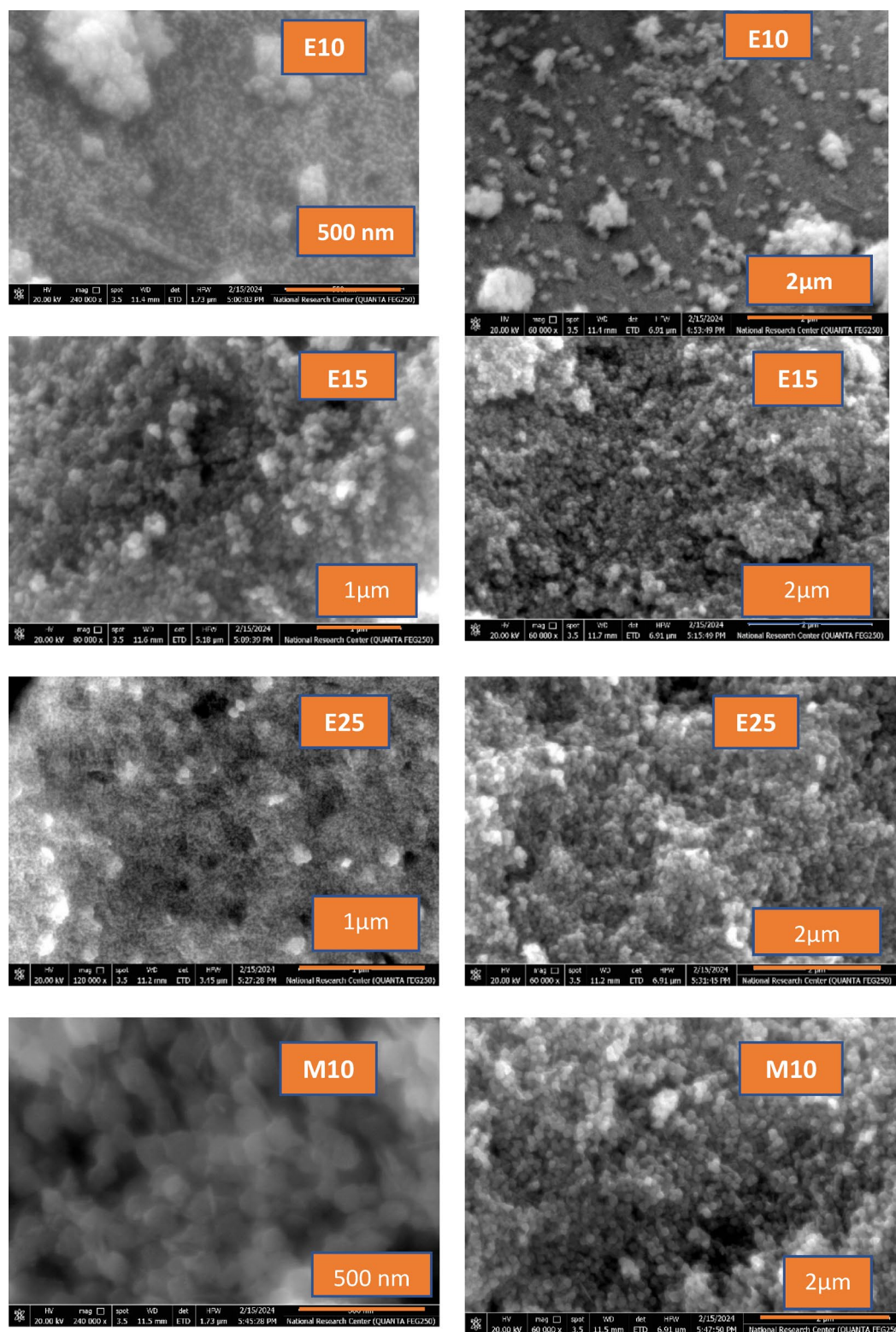


**Fig. 1.** SEM images of ethanol- and methanol-imprinted samples (E10, E15, E25, and M10).

to atomic percentages of 36.75%, 45.52%, and 17.72%, respectively. The finer particle size observed in the M10 sample, corroborated by the EDX data, suggests a higher surface area available for gas interaction. Furthermore, the increased carbon content in M10 may enhance sensor sensitivity by providing additional reactive sites for gas adsorption, thereby improving gas detection efficiency<sup>32</sup>.

When comparing the imprinting effects of ethanol and methanol, the methanol-imprinted samples exhibit significantly finer particle sizes than their ethanol-imprinted counterparts. This suggests that methanol plays

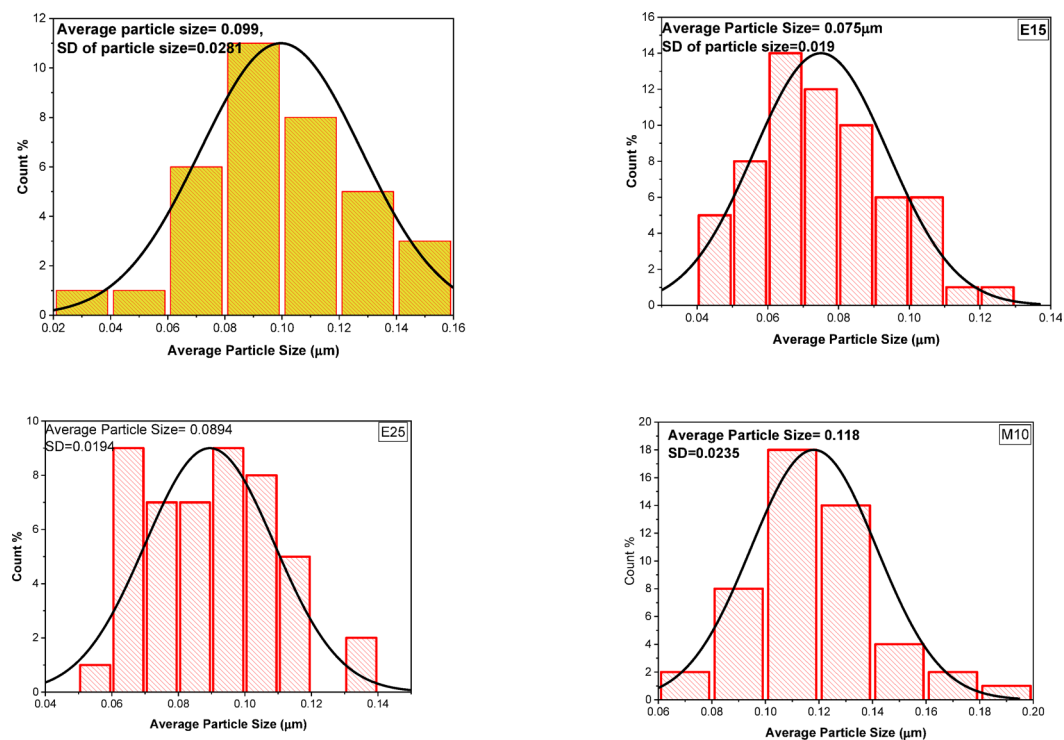


**Fig. 2.** Histogram of particle size distribution and standard deviation for the ethanol- and methanol-imprinted samples (E10, E15, E25, and M10).

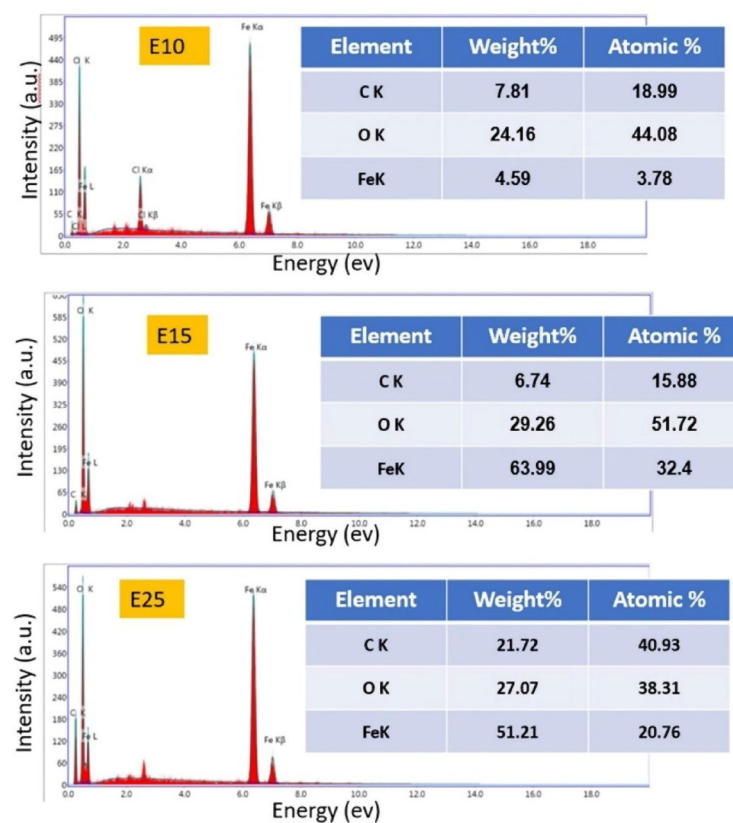


**Fig. 3.** EDX spectra showing weight and atomic percentages of elements in samples E10, E15, and E25.



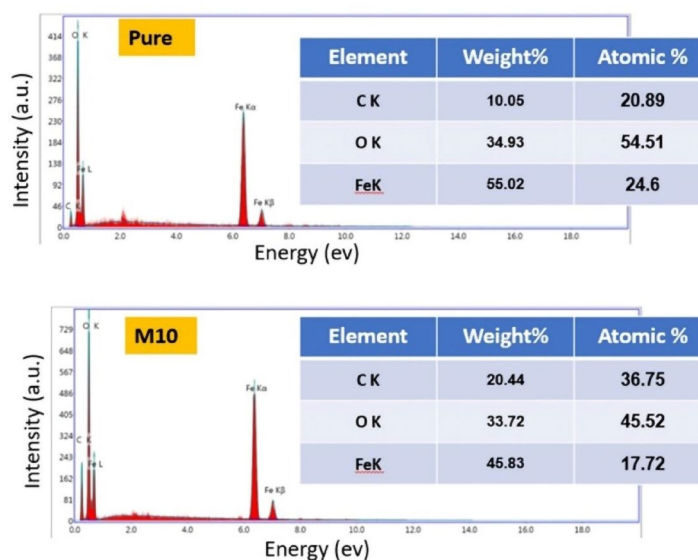


**Fig. 4.** EDX spectra showing weight and atomic percentages of elements in samples pure, and M10.

a more substantial role in particle size reduction, potentially due to its ability to facilitate a more uniform and controlled nucleation process during synthesis. This results in smaller and more homogeneously distributed particles<sup>33</sup>. Consequently, methanol-imprinted sensors are expected to demonstrate superior gas sensing performance due to their increased surface area and enhanced gas adsorption capabilities. This aligns with the observed higher responses in gas sensing tests for methanol-imprinted sensors, further validating their effectiveness in gas detection applications.

#### X-ray diffraction XRD analysis

The X-ray diffraction (XRD) analysis of the ethanol-imprinted nanomaterials (E10, E15, and E25) revealed distinct diffraction patterns with varying peak intensities. All diffraction peaks observed in the synthesized  $\alpha$ -Fe<sub>2</sub>O<sub>3</sub> samples were consistent with the reference pattern for pure  $\alpha$ -Fe<sub>2</sub>O<sub>3</sub> crystal phases (JCPDS: 87–1164), indicating the absence of impurity phases. This confirms the high purity and successful synthesis of  $\alpha$ -Fe<sub>2</sub>O<sub>3</sub> nanomaterials.

The diffraction peaks identified for the E10 sample corresponded to the crystallographic planes (012), (104), (110), (113), (202), (024), (116), (112), (214), (300), (1010), and (036). In contrast, the E15 sample exhibited peaks at (012), (104), (110), (113), (024), (116), (214), (300), (1010), and (036), with a slight reduction in the number of detected peaks. The E25 sample displayed diffraction peaks at (012), (104), (110), (113), (024), (116), (214), (300), and (220), as illustrated in Fig. 5. These results suggest that increasing the ethanol concentration in the imprinting process influences the crystallinity and preferred orientation of the  $\alpha$ -Fe<sub>2</sub>O<sub>3</sub> structure.

Similarly, Fig. 6 presents the XRD analysis of the methanol-imprinted samples (M10, M15, and M25), revealing variations in their diffraction patterns. The M10 sample displayed peaks at (012), (104), (110), (113), (202), (024), (116), (112), (214), (300), and (1010), whereas the M15 sample exhibited peaks at (012), (104), (110), (113), (024), (116), (214), and (300). The M25 sample showed peaks at (012), (104), (113), (024), (116), (214), and (300). Notably, the intensity of the diffraction peaks remained relatively consistent across all methanol-imprinted samples, suggesting that the methanol imprinting process does not significantly alter the crystalline phase of  $\alpha$ -Fe<sub>2</sub>O<sub>3</sub> but may affect its microstructural properties.

These findings indicate that the imprinting process with ethanol and methanol influences the crystalline structure and grain size of  $\alpha$ -Fe<sub>2</sub>O<sub>3</sub> nanomaterials, which may impact their gas-sensing performance. The variation in crystallite size, as shown in Table 2, further supports the hypothesis that imprinting ratios play a role in modifying the structural properties of the nanomaterials, potentially affecting their adsorption behavior and sensing efficiency.

The intensity of the diffraction peaks follows a distinct trend among the ethanol-imprinted samples, with E25 exhibiting the highest intensity, followed by E15, while E10 displays the lowest peak intensity. This variation in peak intensities is attributed to the differing ethanol concentrations in each sample. A higher ethanol content enhances crystallinity and structural ordering, leading to more pronounced diffraction peaks. In the E25 sample, the increased ethanol concentration may facilitate better crystallite alignment and uniform crystal formation, resulting in a noticeable increase in peak intensity. Conversely, the lower ethanol content in E10 may contribute to less defined crystallite structures, thereby reducing the intensity of the XRD peaks.

Additionally, the disappearance of certain diffraction peaks in E15 and E25 compared to E10 could be attributed to changes in crystal orientation or phase composition influenced by ethanol concentration<sup>34</sup>, as shown in Fig. 5. As the ethanol content increases, some crystallographic planes may become more dominant while others diminish, leading to the selective attenuation of specific peaks. This observation suggests that

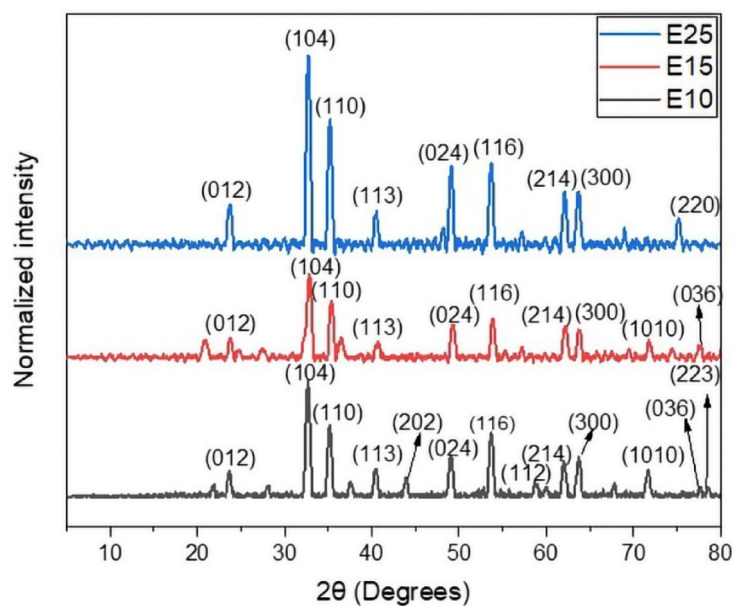


**Fig. 5.** X-ray Diffraction (XRD) patterns of the imprinted samples treated with ethanol.

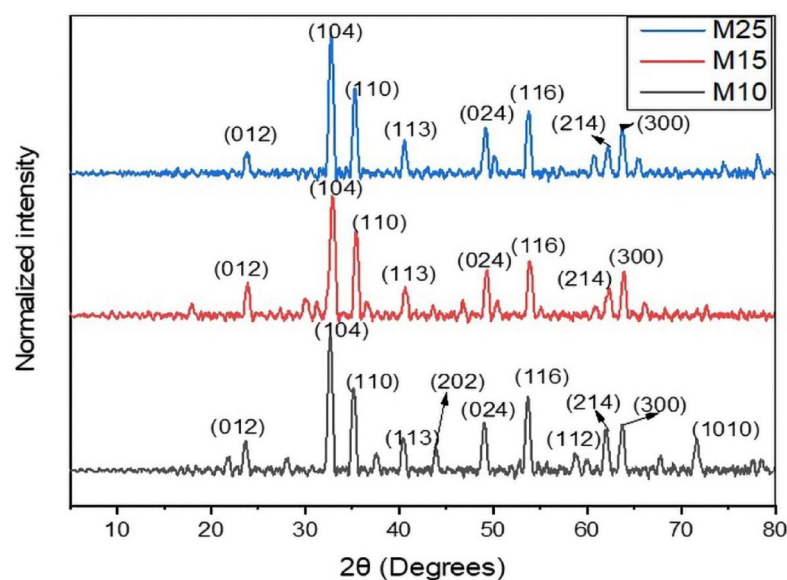


**Fig. 6.** X-ray Diffraction (XRD) patterns of the imprinted samples treated with Methanol.

Sample	Crystalline size
E10	20.673 nm
E15	15.41 nm
E25	22.41393 nm
M10	20.33253 nm
M15	18.5226 nm

**Table 2.** Crystallite (Grain) size from XRD.

ethanol concentration plays a significant role in determining the crystal structure and phase stability of the  $\alpha\text{-Fe}_2\text{O}_3$  samples.

The broad full width at half maximum (FWHM) of the diffraction peaks suggests the presence of small crystallite sizes, which were estimated using Scherrer's equation<sup>35</sup>:

$$D = \frac{K\lambda}{\beta \cos \theta} \quad (3)$$

where  $D$  represents the crystallite size,  $\theta$  is the Bragg angle in radians,  $\beta$  denotes the full width at half maximum (FWHM),  $\lambda$  is the X-ray wavelength (1.5406 Å), and  $K$  is Scherrer's constant. The crystallite sizes calculated for the (104) diffraction plane are approximately 20.6 nm, 15.41 nm, 22.41 nm, 20.33 nm, 18.52 nm, and 15.62 nm for E10, E15, E25, M10, M15, and M25, respectively, as detailed in Table 2.

The variation in crystallite size significantly influences the gas-sensing performance, as smaller nanoparticles provide a higher specific surface area, which enhances sensor sensitivity. The ethanol-imprinted samples (E10, E15, E25) exhibit an initial decrease in crystallite size (E15: 15.41 nm) before increasing at higher ethanol concentrations (E25: 22.41 nm). In contrast, the methanol-imprinted samples (M10, M15, M25) show a more consistent reduction in crystallite size with increasing methanol concentration, decreasing from 20.33 nm (M10) to 15.62 nm (M25). These findings suggest that both ethanol and methanol influence the nucleation and growth kinetics of the nanomaterial, with ethanol exhibiting a more variable effect on crystallite formation, while methanol demonstrates a steadier trend in reducing crystallite size at higher concentrations.

#### FTIR analysis

The FTIR spectra of the ethanol-imprinted samples (E10, E15, and E25) presented in Fig. 7 reveal distinct stretching peaks, indicating the presence of specific functional groups and bonding environments within the synthesized hematite ( $\alpha\text{-Fe}_2\text{O}_3$ ) nanomaterials. The variation in ethanol concentration during synthesis influences the observed vibrational modes, providing insights into structural modifications and molecular interactions.

For the E10 sample, characteristic stretching peaks appear at 3035, 1616, 1428, 941, 798, 518, and 430  $\text{cm}^{-1}$ . The broad peak at 3035  $\text{cm}^{-1}$  corresponds to O–H stretching, confirming the presence of residual ethanol. The peaks at 1616  $\text{cm}^{-1}$  and 1428  $\text{cm}^{-1}$  are associated with C=C stretching and  $\text{CH}_2$  bending vibrations, respectively, suggesting the presence of aliphatic or aromatic structures. Peaks at 941  $\text{cm}^{-1}$  and 798  $\text{cm}^{-1}$  correspond to C–H bending vibrations, while the lower frequency peaks at 518  $\text{cm}^{-1}$  and 430  $\text{cm}^{-1}$  are attributed to Fe–O stretching, confirming the formation of iron oxide.

For the E15 sample, stretching peaks are observed at 2957, 1615, 1428, 941, 892, 800, 514, and 425  $\text{cm}^{-1}$ . The peak at 2957  $\text{cm}^{-1}$  corresponds to O–H stretching, indicative of ethanol presence. The 1615  $\text{cm}^{-1}$  peak is linked to C=C stretching, while the 1428  $\text{cm}^{-1}$  peak corresponds to  $\text{CH}_2$  bending vibrations. Peaks at 941  $\text{cm}^{-1}$  and 892  $\text{cm}^{-1}$  indicate C–H bending vibrations, with the 800  $\text{cm}^{-1}$  peak suggesting C–H bending in aromatic compounds. The Fe–O stretching vibrations are confirmed by peaks at 514  $\text{cm}^{-1}$  and 425  $\text{cm}^{-1}$ , reinforcing the presence of iron oxide.

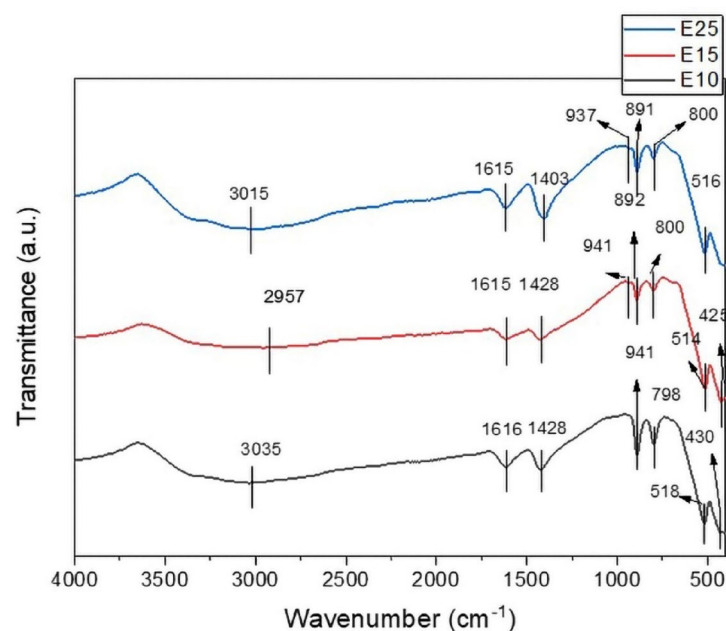


**Fig. 7.** FTIR spectra of the samples E10, E15, and E25.

For the E25 sample, stretching peaks appear at 3015, 1615, 1403, 937, 891, 800, and 516  $\text{cm}^{-1}$ . The 3015  $\text{cm}^{-1}$  peak corresponds to O–H stretching, further confirming the role of ethanol in synthesis. The 1615  $\text{cm}^{-1}$  peak is associated with C=C stretching, while the 1403  $\text{cm}^{-1}$  peak corresponds to  $\text{CH}_2$  bending vibrations. Peaks at 937  $\text{cm}^{-1}$  and 891  $\text{cm}^{-1}$  suggest C–H bending vibrations, and the peak at 800  $\text{cm}^{-1}$  is attributed to C–H bending in aromatic compounds. The 516  $\text{cm}^{-1}$  peak is linked to Fe–O stretching vibrations, further verifying the formation of the  $\alpha\text{-Fe}_2\text{O}_3$  phase.

These FTIR results confirm the successful synthesis of hematite nanomaterials while providing insights into the molecular interactions influenced by ethanol imprinting. The presence of Fe–O bonds across all samples validates the formation of the iron oxide phase, while variations in C–H and O–H vibrations suggest modifications in surface chemistry due to ethanol concentration differences. These structural variations are likely to impact the gas-sensing properties of the materials, influencing their adsorption characteristics and sensor performance.

The FTIR spectra of the methanol-imprinted samples (M10, M15, and M25) presented in Fig. 8 exhibit distinct stretching peaks, indicating the presence of specific functional groups and bonding environments within the synthesized hematite ( $\alpha\text{-Fe}_2\text{O}_3$ ) nanomaterials. The variation in methanol concentration during synthesis influences the vibrational modes, providing insights into structural modifications and surface chemistry.

For the M10 sample, characteristic stretching peaks are detected at 3107, 2352, 1624, 1435, 891, 798, 525, and 430  $\text{cm}^{-1}$ . The broad peak at 3107  $\text{cm}^{-1}$  corresponds to O–H stretching, confirming the presence of residual methanol. The peak at 2352  $\text{cm}^{-1}$  is typically associated with  $\text{CO}_2$  adsorption, indicating possible atmospheric interactions with the sample surface. The 1624  $\text{cm}^{-1}$  peak corresponds to C=C stretching, while the 1435  $\text{cm}^{-1}$  peak is attributed to  $\text{CH}_2$  bending vibrations. Peaks at 891  $\text{cm}^{-1}$  and 798  $\text{cm}^{-1}$  correspond to C–H bending vibrations, and the peaks at 525  $\text{cm}^{-1}$  and 430  $\text{cm}^{-1}$  confirm Fe–O stretching, validating the formation of iron oxide.

For the M15 sample, stretching peaks are observed at 3114, 3017, 1761, 1617, 1396, 1042, 1009, 935, 515, and 421  $\text{cm}^{-1}$ . The peaks at 3114  $\text{cm}^{-1}$  and 3017  $\text{cm}^{-1}$  correspond to O–H stretching, confirming methanol's role in synthesis. The 1761  $\text{cm}^{-1}$  peak is associated with C=O stretching, which may indicate the presence of adsorbed carbonyl-containing species. The 1617  $\text{cm}^{-1}$  peak corresponds to C=C stretching, while the 1396  $\text{cm}^{-1}$  peak is linked to  $\text{CH}_2$  bending vibrations. Peaks at 1042  $\text{cm}^{-1}$  and 1009  $\text{cm}^{-1}$  suggest C–O stretching, while the peak at 935  $\text{cm}^{-1}$  is attributed to C–H bending vibrations. The peaks at 515  $\text{cm}^{-1}$  and 421  $\text{cm}^{-1}$  confirm Fe–O stretching, reinforcing the formation of the hematite phase.

For the M25 sample, stretching peaks appear at 3115, 3021, 2802, 1753, 1619, 1396, and 518  $\text{cm}^{-1}$ . The peaks at 3115  $\text{cm}^{-1}$  and 3021  $\text{cm}^{-1}$  correspond to O–H stretching, confirming methanol's influence on synthesis. The 2802  $\text{cm}^{-1}$  peak suggests the presence of aldehyde C–H stretching, indicating possible surface modifications. The 1753  $\text{cm}^{-1}$  peak corresponds to C=O stretching, and the 1619  $\text{cm}^{-1}$  peak is attributed to C=C stretching. The 1396  $\text{cm}^{-1}$  peak corresponds to  $\text{CH}_2$  bending vibrations, while the peak at 518  $\text{cm}^{-1}$  is associated with Fe–O stretching, further validating the formation of hematite.

The FTIR spectra confirms the presence of methanol-derived O–H stretching and characteristic Fe–O vibrations, demonstrating how varying methanol concentrations influence the molecular environment and composition of the synthesized hematite nanomaterials. Differences in peak positions and intensities suggest that higher methanol concentrations in M15 and M25 introduce additional functional groups and possibly adsorbed species. These variations in surface chemistry may have a direct impact on the material's properties, particularly in gas-sensing applications, where functional group interactions play a crucial role in adsorption and detection performance.

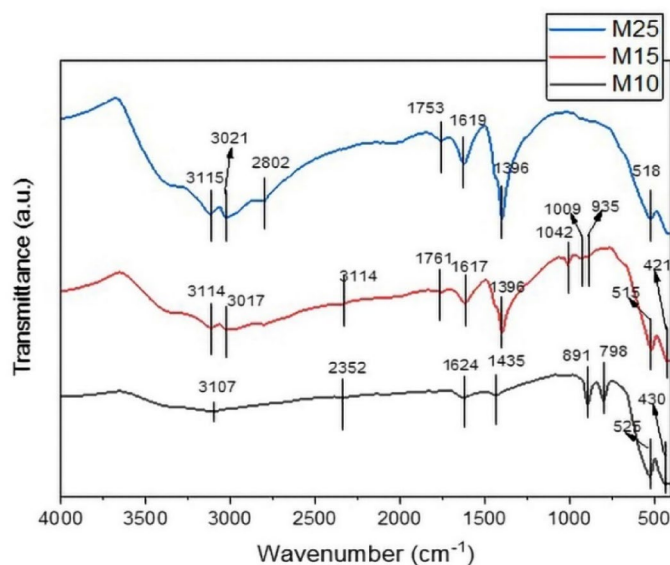


**Fig. 8.** FTIR spectra of samples M10, M15, and M25.



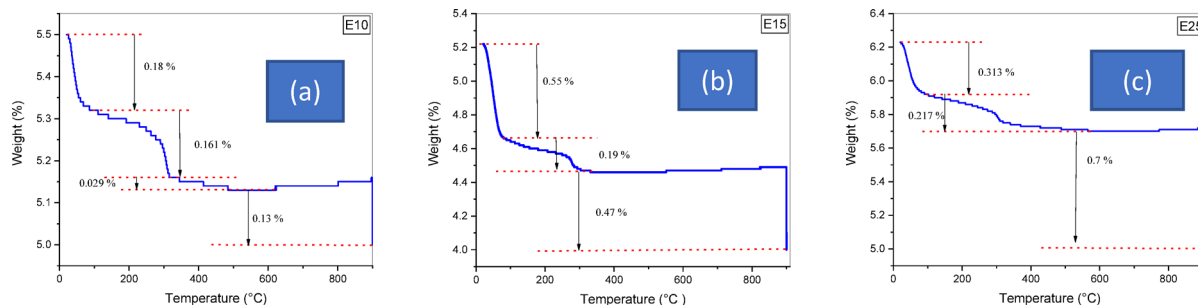


**Fig. 9.** Thermogravimetric Analysis (TGA) curves for samples (a) E10, (b) E15, and (c) E25.

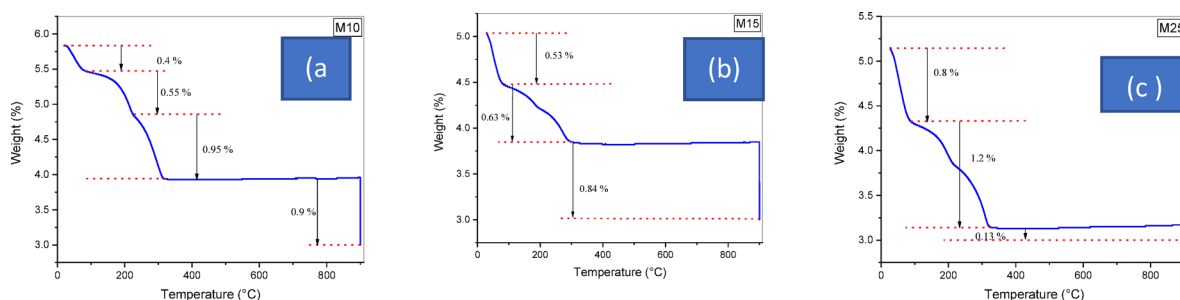


**Fig. 10.** Thermogravimetric Analysis (TGA) curves for samples (a) M10, (b) M15, and (c) M25.

#### Thermogravimetric analysis (TGA)

Figure 9 presents the Thermogravimetric Analysis (TGA) curves for the ethanol-imprinted samples (E10, E15, and E25), illustrating their thermal stability by analyzing weight loss across different temperature ranges.

The E10 sample exhibits the least overall weight loss, with a minimal reduction of 0.18% from 0 to 100 °C, 0.16% from 100 to 300 °C, 0.29% from 300 to 500 °C, and 0.13% from 500 to 900 °C. This suggests that E10 possesses high thermal stability, with minimal residual moisture and organic content that decomposes at elevated temperatures. The limited weight loss indicates a relatively pure and well-structured hematite nanomaterial, confirming the effectiveness of the synthesis process in minimizing residual organic components.

In contrast, the E15 sample undergoes more significant weight losses, particularly 0.55% from 0 to 100 °C and 0.47% from 300 to 900 °C, indicating the presence of a higher proportion of volatile organic residues and ethanol-derived compounds. The increased weight loss in E15 suggests that residual organic species remain trapped within the material, potentially influencing its surface chemistry and gas adsorption properties.

The E25 sample demonstrates an intermediate level of thermal stability, with weight losses of 0.313% from 0 to 100 °C, 0.217% from 100 to 300 °C, and 0.7% from 300 to 900 °C. The relatively higher weight loss at elevated temperatures suggests that E25 contains a notable amount of volatile components that decompose progressively with increasing temperature.

Overall, the TGA analysis confirms that the E10 sample exhibits the highest thermal stability, undergoing the least thermal decomposition. This suggests a cleaner synthesis process with minimal residual organic contaminants. The observed differences in thermal behavior among the samples indicate that ethanol concentration during synthesis influences the material's composition and thermal stability, which may have implications for its long-term durability and gas-sensing performance.

For the methanol-imprinted hematite samples, the TGA curves presented in Fig. 10 provide insights into their thermal stability by analyzing weight loss across different temperature ranges. The M10 sample exhibits weight losses of 0.4% from 0 to 100 °C, 0.55% from 200 to 300 °C, and 0.9% from 300 to 900 °C. These results indicate a gradual decomposition pattern, likely associated with the evaporation of residual methanol embedded during the synthesis process. The relatively low weight loss suggests that M10 maintains a more stable thermal profile, with minimal volatile organic residue.

The M15 sample shows slightly higher weight losses of 0.53% from 0 to 100 °C, 0.63% from 100 to 300 °C, and 0.84% from 300 to 900 °C. This suggests an increased decomposition rate compared to M10, potentially due to the higher methanol imprinting ratio, which may have resulted in a greater retention of organic compounds that volatilize at elevated temperatures.

The M25 sample displays the highest weight loss among the methanol-imprinted samples, with 0.8% from 0 to 100 °C, 1.2% from 100 to 300 °C, and 0.13% from 300 to 900 °C. This pronounced weight reduction, particularly at lower temperatures, indicates a substantial presence of volatile organic residues, likely derived from methanol compounds. The significant decomposition at early stages suggests that M25 exhibits lower thermal stability compared to M10 and M15, with increased susceptibility to organic residue volatilization at higher methanol concentrations.

Overall, based on TGA analysis, the E10 and M10 samples demonstrate relatively stable thermal properties compared to their counterparts E15, E25, M15, and M25. Both E10 and M10 exhibit lower overall weight loss percentages, indicating a cleaner synthesis process with fewer residual organic contaminants and more stable decomposition characteristics across the tested temperature ranges. These findings suggest that lower ethanol and methanol imprinting ratios contribute to enhanced thermal stability, which may influence the long-term durability and gas-sensing performance of the synthesized hematite nanomaterials.

#### FL (Fluorescence) analysis

In its bulk state,  $\alpha\text{-Fe}_2\text{O}_3$  exhibits an absence of photoluminescent (PL) emission when stimulated by a 350 nm laser. However, the photoluminescence spectrum of the synthesized  $\alpha\text{-Fe}_2\text{O}_3$  nanoparticles, as presented in Fig. 11, reveals broad and prominent PL peaks around 703 nm. The recorded emission intensities are 250 arbitrary units (a.u.) for sample E15 and 290 a.u. for sample M15, indicating variations in defect density and structural properties.

The higher PL intensity observed in M15 suggests a lower defect density compared to E15. A lower defect density reduces non-radiative recombination centers, enhancing radiative recombination and thus increasing the emission intensity. This can be attributed to the capping effect of the imprinting molecules during synthesis, which stabilize the surface and prevent defect formation<sup>33</sup>.

Defect density directly affects gas-sensing performance, as a lower defect density improves the stability of surface states, enhances charge carrier mobility, and provides a more reliable interaction with gas molecules. Consequently, the M15 sample, with its lower defect density, is expected to exhibit a higher and more stable gas response compared to E15, which has more surface defects leading to instability in gas adsorption and desorption processes.

The distinctive structural characteristics of  $\alpha\text{-Fe}_2\text{O}_3$  in its nanoscale form, along with the inclusion of imprinting agents as surface modifiers, contribute to the observed quantum confinement effects and surface state modifications.

According to the Pauling-Hendricks model for hematite, an increased separation of Fe–O bonds, modifications in oxygen atom coordination, and enhanced magnetic coupling between neighboring  $\text{Fe}^{3+}$  ions influence the photoluminescent behavior<sup>34</sup>. The observed emission is likely due to bound-exciton recombination, evidenced by the large Stokes shift between excitation and emission wavelengths.

These findings suggest that imprinting with methanol (M15) not only improves the optical properties but also enhances gas-sensing performance by lowering the defect density and stabilizing surface properties.

#### Electrical properties analysis and data curation

The electrical properties of the synthesized  $\alpha\text{-Fe}_2\text{O}_3$  nanoparticles, imprinted with varying concentrations of ethanol and methanol, were systematically analyzed through current–voltage (I–V) characterization, temperature response, and gas sensing performance. These investigations are critical in assessing the suitability of these nanoparticles for potential Internet of Things (IoT) applications in real-time gas monitoring and environmental sensing.

#### I–V Characterization investigation

The I–V characteristics of the fabricated sensor devices were examined using a METROHM Autolab 87,070 Potentiostat system, applying a bias voltage range of  $\pm 5$  V. The resulting I–V curves are presented in Figs. 12 and 13, while the electrical resistance values for the different sensor devices are summarized in Table 3.

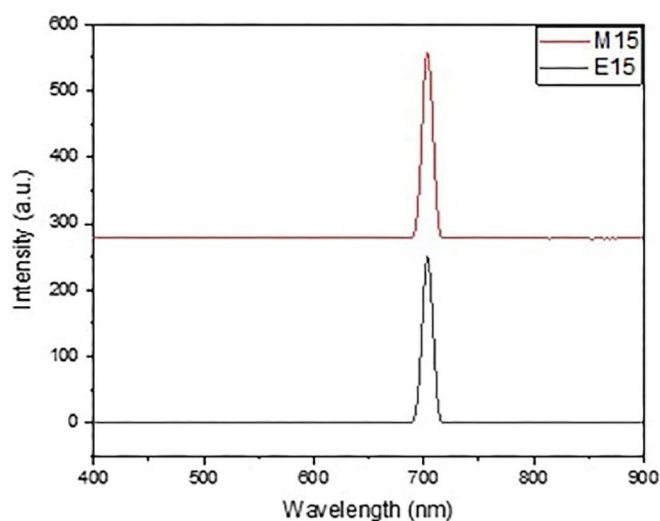


**Fig. 11.** Photoluminescence measurements of the samples (E15, M15).

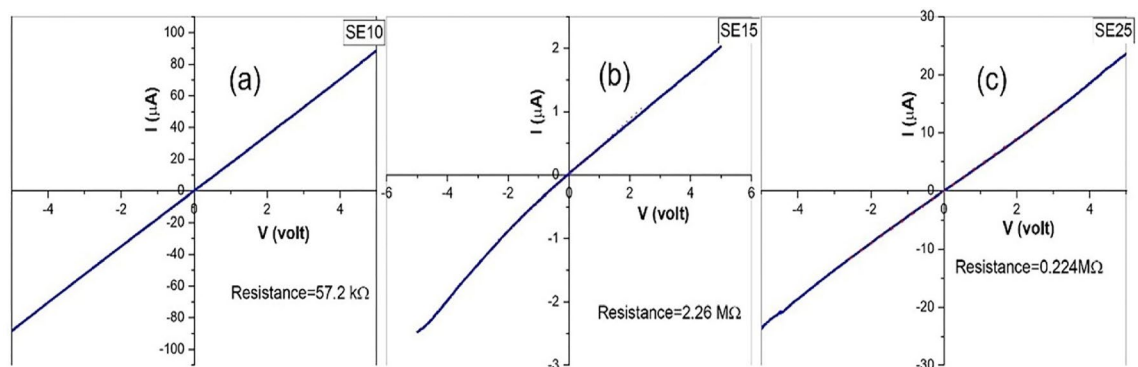


**Fig. 12.** The I-V characteristic plots for the linear devices are shown as (a) SE10, (b) SE15, and (c) SE25 under  $\pm 5$  V forward and reverse bias.

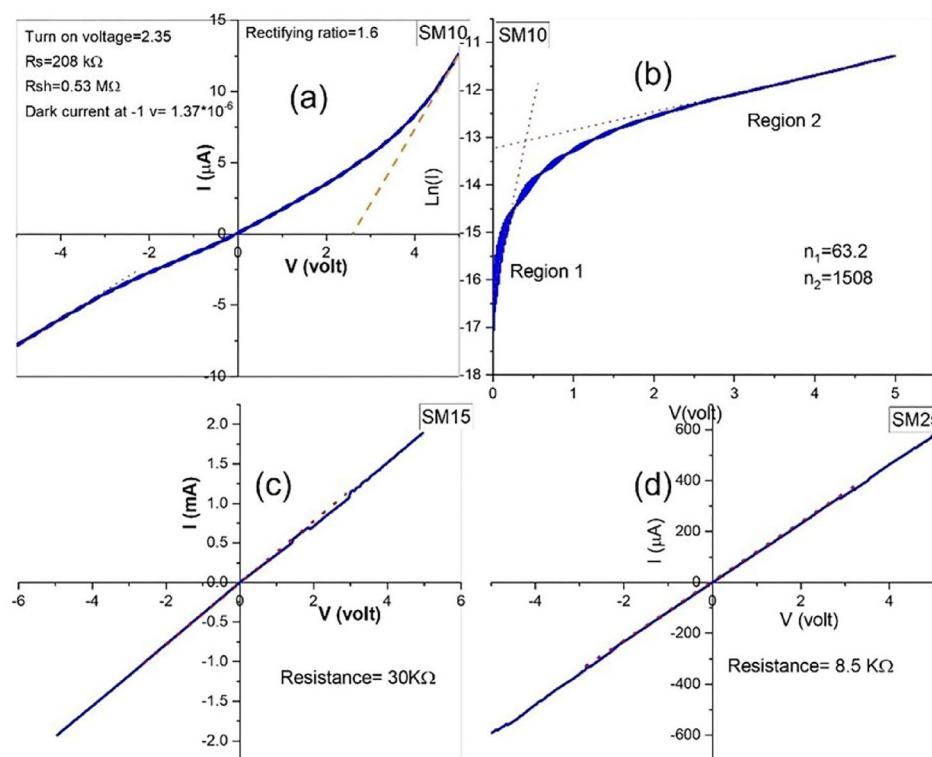


**Fig. 13.** The I-V characteristic plots for the nonlinear sample (a) M10, (b) LN(I) vs V(volts), (c) linear sample M15, and (d) M25 under  $\pm 5$  V forward and reverse bias.

Sensor symbol	Resistance
SE10	57.2 k $\Omega$
SE15	2.26 M $\Omega$
SE25	0.224 M $\Omega$
SM15	30 k $\Omega$
SM25	8.5 k $\Omega$

**Table 3.** Resistance measurements for the sensors exhibiting linear behavior.

The ethanol-imprinted sensors SE10, SE15, and SE25 exhibited ohmic behavior, with resistances of 57.2 k $\Omega$ , 2.26 M $\Omega$ , and 0.224 M $\Omega$ , respectively. The observed linear current–voltage relationship suggests efficient charge carrier transport across the junctions with minimal barrier potential. Notably, SE10 demonstrated the lowest resistance, indicating superior electrical conductivity compared to SE15 and SE25. This difference may be attributed to variations in material composition, crystallinity, or junction quality, which influence charge mobility and interfacial properties. Additionally, methanol-imprinted sensors SM15 and SM25 exhibited resistance values of 30 k $\Omega$  and 8.5 k $\Omega$ , respectively, further indicating differences in electrical performance based on imprinting conditions.

In contrast, sensor SM10 displayed a rectifying I–V response, as illustrated in Fig. 13, functioning as a rectifying diode with a turn-on voltage of 2.35 V, a dark current of  $1.37 \times 10^{-6}$  A at  $-1$  V, a rectifying ratio of 1.6, and series ( $R_s$ ) and shunt ( $R_{sh}$ ) resistances of 208 k $\Omega$  and 0.5 M $\Omega$ , respectively. This rectifying behavior arises from the formation of a Schottky barrier at the metal–semiconductor interface, which restricts charge carrier flow in one direction while facilitating it in the other. Several factors contribute to this behavior in SM10, including differences in metal work function, semiconductor doping levels, and interface states, all of which influence barrier height and charge transport dynamics.

To further evaluate the diode characteristics, the Schottky diode equation was applied to determine the quality factors in both low voltage (Region 1) and high voltage (Region 2)<sup>30</sup>, as shown in Fig. 13:

$$I_D = I_S \left[ e^{\frac{V_D}{nKT}} - 1 \right] \quad (4)$$

where:

- $I_D$  is the diode current,
- $I_S$  is the reverse saturation current,
- $V_D$  is the applied voltage,
- $n$  is the ideality factor (quality factor),
- $K$  is the Boltzmann constant,
- $T$  is the absolute temperature.

The slope of the  $\ln(I)$  vs.  $V$  curve was used to determine the quality factor values, while the series resistance ( $R_s$ ) and shunt resistance ( $R_{sh}$ ) for SM10 were also calculated. The finding that  $R_{sh} > R_s$  confirms that the device operates within stable conditions, ensuring consistent performance.

These electrical characterizations provide crucial insights into the charge transport mechanisms within the fabricated sensor devices and highlight the influence of ethanol and methanol imprinting on sensor conductivity, rectification behavior, and potential application in gas sensing technologies.

#### *Gas sensing performance for Fe<sub>2</sub>O<sub>3</sub>-Doped (MIT) gas sensors*

The fabricated gas sensors were evaluated for their response to ethanol and methanol vapors, with ethanol-imprinted sensors tested for ethanol detection and methanol-imprinted sensors tested for methanol detection. This methodology was employed to examine the impact of molecular imprinting on gas response and to determine the optimal imprinting ratio for enhanced sensor performance. The gas-sensing experiments were conducted at a fixed gas concentration of 100 ppm under environmental conditions with absolute humidity ranging from 40 to 60 g/m<sup>3</sup>. Additionally, the sensor response was analyzed across a temperature range of 30 to 300 °C to assess the influence of temperature on sensor performance.

To ensure the reliability and long-term stability of the fabricated sensors, their reproducibility and repeatability were examined through a single calibration experiment lasting approximately 12 h, repeated five times over a span of 60 days. This assessment confirmed the ability of the sensors to maintain consistent and stable responses under controlled conditions.

As depicted in Fig. 14a, among the ethanol-imprinted sensors, SE10 exhibited the highest response of 92% at 100 °C, followed by SE25 with 82% at 120 °C, and SE15 with 68% at 200 °C. In comparison, the pure (non-imprinted) sample demonstrated a response of 47% at 130 °C, significantly lower than the imprinted sensors.

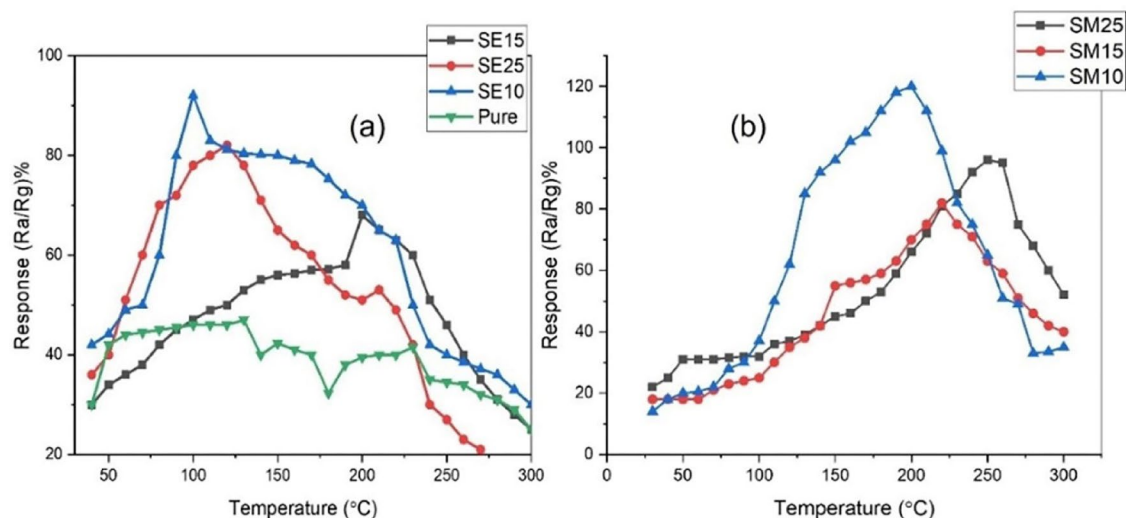
Similarly, for the methanol-imprinted sensors, as shown in Fig. 14b, SM10 displayed the highest response of 120% at 200 °C, followed by SM25 with 96% at 250 °C, and SM15 with 82% at 220 °C. These findings align with the I–V characterization results, reinforcing the reliability of the experimental outcomes.

Interestingly, the gas response did not increase linearly with the imprinting ratio. The highest responses were observed for sensors with a 10% imprinting ratio for both ethanol (SE10) and methanol (SM10), suggesting that a moderate imprinting ratio provides optimal performance. Additionally, SE10 exhibited a strong response at a relatively low operating temperature of 100 °C, making it particularly suitable for applications requiring low-power consumption and reduced thermal stress. Likewise, SM10, imprinted with methanol, provided the highest response at 200 °C, demonstrating effective performance at a moderate operating temperature compared to other methanol-imprinted sensors.

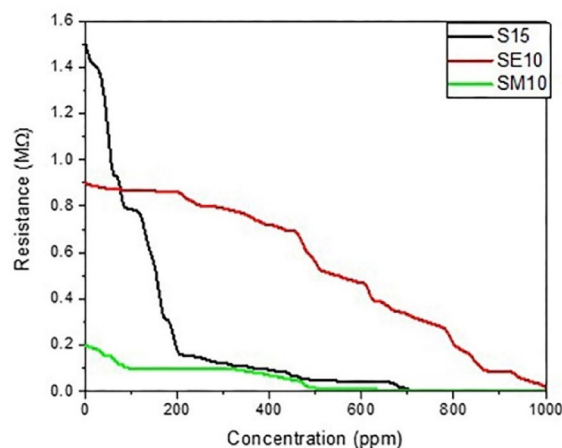
Overall, the methanol-imprinted sensors exhibited superior gas sensing performance compared to ethanol-imprinted counterparts, emphasizing their greater efficiency and applicability for gas detection. The variations in response among different imprinting ratios highlight the importance of optimizing nanomaterial imprinting conditions to achieve the best sensing performance.

Figure 15 illustrates the relationship between resistance and gas concentration at room temperature for selected sensors (SM10, SE10, and S15), further validating their sensing capabilities and performance consistency.





**Fig. 14.** Response change Versus Temperature (°C) (a) for Ethanol imprinted devices, (b) for Methanol imprinted devices.



**Fig. 15.** Resistance versus gas concentration at room temperature for sensor array (SM10, SE10, and S15).

Figure 16 illustrates the relationship between sensor resistance ( $R_g$ ) and gas concentration at room temperature for three different gas sensors: SM10, SE10, and S15. The initial resistances of these sensors in air were measured as 0.2 MΩ for SM10, 0.9 MΩ for SE10, and 1.5 MΩ for S15, where S15 is an acetone-imprinted sensor with a 15% imprinting ratio.

As gas concentration increases, the resistance of each sensor decreases, a trend that can be attributed to the interaction between gas molecules and the sensor surface, which enhances charge carrier density. This improved charge mobility subsequently increases the sensor's electrical conductivity, leading to a reduction in resistance. The observed performance of the sensor array validates its effectiveness in real-time gas detection, a critical aspect for applications in gas sensing and environmental monitoring.

Figure 16 presents the output voltage response of the gas sensors as a function of gas concentration, ranging from 0 to 2500 ppm, for the three sensor devices integrated into the electronic nose (e-nose) system. Among the tested sensors, the Sp sensor (acetone-imprinted and palladium-doped) exhibits the highest slope, indicating the most significant response to gas concentration changes. This sensor demonstrates the highest sensitivity, followed by SM10 in second place and SE10 in third place.

The Sp sensor is characterized by two key enhancements: acetone imprinting and palladium doping. The acetone-imprinting process involves creating specific molecular recognition sites within the sensor's structure, which allows the sensor to preferentially interact with acetone molecules. This selective binding is achieved by incorporating acetone during the synthesis process, ensuring the sensor responds more effectively to acetone exposure. The imprinting procedure involves heating a mixture of acetone,  $\text{FeCl}_3 \cdot 6\text{H}_2\text{O}$ , and palladium salt ( $\text{PdSO}_4$ ) in a Teflon-lined autoclave at 130 °C for 90 min, resulting in the formation of acetone-specific sites.

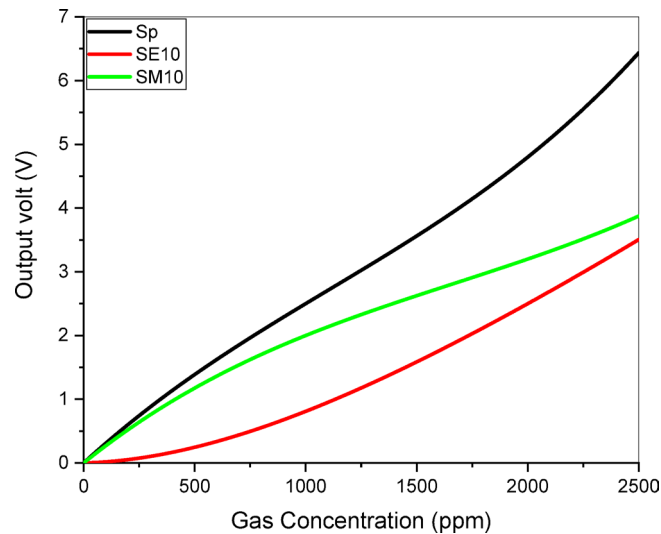


Fig. 16. Output volt versus gas concentration.

Sensor device	Mathematical model of sensor response derived from voltage versus gas concentration curves
Sp	$y = -1E-19x^6 + 1E-15x^5 - 5E-12x^4 + 1E-08x^3 - 1E-05x^2 + 0.007x - 0.1153$
SE10	$y = -8E-20x^6 + 6E-16x^5 - 1E-12x^4 - 1E-10x^3 + 1E-06x^2 + 0.0012x + 0.064$
SM10	$y = 7E-20x^6 - 5E-16x^5 + 1E-12x^4 - 2E-09x^3 + 1E-06x^2 + 0.0002x + 0.1236$

Table 4. Mathematical model of output voltage vs. gas concentration for each sensor in the sensor array.

Palladium doping is used to further enhance the sensor’s electrical properties and catalytic activity. Palladium salt (PdSO4, 0.1 g) is dissolved in HCl and combined with FeCl<sub>3</sub>·6H<sub>2</sub>O and acetone. The resulting solution undergoes a process where ammonium hydroxide is added, and the mixture is stirred to reach a pH of 11. The acetone template is then sealed and heated at 130 °C, and after centrifugation and washing, the product is dried and ground to create the final sensor material. The rationale for incorporating 0.1 g of palladium is its known ability to enhance conductivity and catalyze the oxidation of acetone, improving the sensor’s response and sensitivity to acetone gas<sup>27</sup>.

Despite differences in response magnitude, all three sensors demonstrated a strong correlation between gas concentration and sensor output, confirming their high sensitivity and reliable detection capabilities. To further quantify this relationship, Table 4 provides 6th-degree polynomial regression models that describe the output voltage response as a function of gas concentration for each sensor. These models were developed using MATLAB through curve fitting techniques, ensuring a precise mathematical representation of sensor behavior.

To enhance the practical application of this e-nose system, artificial intelligence (AI) algorithms were implemented to analyze the dataset, which includes output voltage versus gas concentration. AI-based models were evaluated to determine the most effective algorithm for making real-time decisions and alerting users when gas concentrations exceed predefined safety thresholds. Specifically, the gas concentration thresholds were set at:

- 500 ppm for acetone and ethanol.
- 200 ppm for methanol.

These AI-driven real-time monitoring and alert mechanisms significantly improve the system’s applicability in industrial safety, environmental monitoring, and smart sensing applications, ensuring user safety and gas exposure prevention.

The results demonstrate that molecular imprinting and sensor doping significantly enhance gas detection performance. The Sp sensor, doped with palladium, exhibited the highest response, confirming its superior sensitivity. The 6th-degree polynomial regression models provide a precise mathematical approach for predicting sensor responses at varying gas concentrations, which, when combined with AI-based decision-making, ensures efficient real-time gas monitoring and enhanced user safety.

Real-time classification and monitoring of gaseous chemicals using machine learning models

The dataset utilized in this study was collected from an electronic nose (e-nose) system comprising three distinct sensors: SE10, SM10, and Sp, selected for their optimal gas detection performance. Each sensor recorded output voltage readings across gas concentrations ranging from 0 to 2500 ppm. The dataset consists of 7503 rows (2501 rows per gas for ethanol, methanol, and acetone) and five columns, encompassing both categorical and numerical variables.

The dataset is structured as follows:

1. Sensor Name – Identifies the sensor used for detection.
2. Sensor Readings – Captures voltage output from each sensor at specific concentrations.
3. Gas Concentration – Represents the recorded gas levels in ppm.
4. Gas Type – Specifies the type of gas detected (ethanol, methanol, or acetone).
5. Gas Condition – Categorizes the detected gas as either 'low' or 'high' based on predefined threshold values (500 ppm for ethanol and acetone, 200 ppm for methanol).

To ensure effective machine learning model training, a preprocessing pipeline was implemented, which included:

- Normalization: Sensor readings and gas concentrations were standardized using StandardScaler, ensuring uniform feature scaling.
- Encoding Categorical Variables: Labels such as sensor names, gas types, and gas conditions were converted into numeric values using LabelEncoder.

Two primary analyses were conducted:

- Classification Analysis – To distinguish between different gas types.
- Regression Analysis – To predict gas concentration levels.

For classification, three features were used: sensor name, sensor readings, and gas concentration levels. The dataset was divided into:

- Training Set – 80% (6002 samples).
- Testing Set – 20% (1501 samples).

The `train_test_split` function (`test_size=0.2`) was used to ensure an effective model evaluation.

The neural network model consisted of:

- Input Layer – Accepting sensor readings and gas concentration data.
- Three Fully Connected Layers:
  - Layer 1 ( $n_1$ ): 32 neurons.
  - Layer 2 ( $n_2$ ): 50 neurons.
  - Layer 3 ( $n_3$ ): 128 neurons.

These layers process the input data through successive transformations.

- Output Layer – Comprising two output nodes, classifying both gas type and gas condition simultaneously.

The performance of the classification model was assessed using the accuracy. For the regression analysis, the following metrics were computed:

- Mean Absolute Error (MAE).
- Mean Squared Error (MSE).
- Root Mean Square Error (RMSE).
- Normalized RMSE (NRMSE).
- Coefficient of Determination ( $R^2$ ).
- Limit of Detection (LOD).
- Limit of Quantification (LOQ).

All machine learning analyses were executed using the TensorFlow 2 framework with Python 3.7 on Kaggle's cloud computing platform. The computational setup included:

- Intel(R) Xeon(R) CPU @ 2.00 GHz.
- 52 GB RAM.
- Tesla T4 16 GB GPU.

This computational environment provided sufficient power for efficient data handling, feature processing, and model training. This figure presents an overview of the AI-driven e-nose system, illustrating how machine learning models analyze sensor data for real-time classification and monitoring of gaseous chemicals.

The electronic nose (E-nose) system is designed to detect and analyze gas concentrations in real-time using AI algorithms. The schematic diagram in Fig. 17 illustrates the system's workflow, which begins with the introduction of the target gas into a test chamber.

#### *System workflow*

##### 1. Gas Exposure and Sensor Response

- Within the test chamber, a set of gas sensors detects acetone, ethanol, and methanol at varying concentrations.

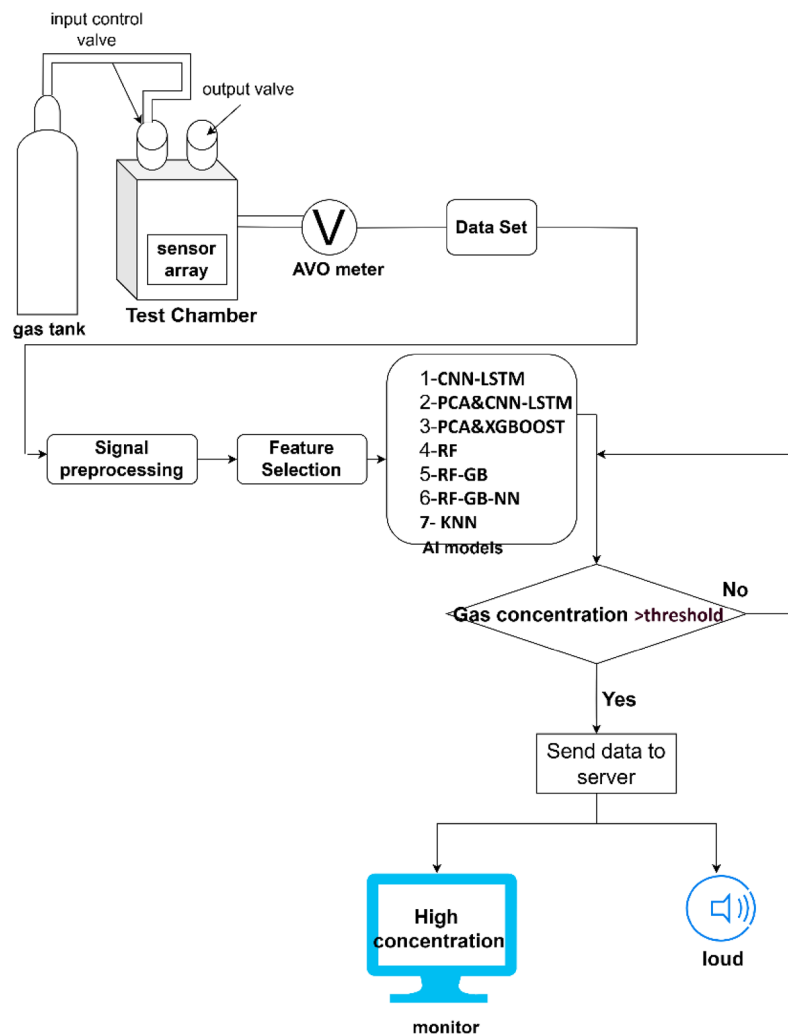


**Fig. 17.** Schematic representation of the electronic nose (E-Nose) system utilizing AI algorithms.

- These sensors measure the gas-sensing response, which is transmitted to an AVO meter that records the corresponding output voltage for each gas concentration.
- The recorded voltage values form the foundation of the dataset for further processing.

## 2. Data Processing and Feature Selection

- The collected sensor data is input into a Python-based program, where it undergoes signal processing to refine the sensor responses and remove noise.
- Feature selection techniques are applied to extract the most relevant attributes for accurate gas detection and classification.

## 3. AI Model Implementation

- The processed dataset is then used to train and test seven AI models, including: CNN-LSTM (Convolutional Neural Network-Long Short-Term Memory).
- PCA & CNN-LSTM (Principal Component Analysis & CNN-LSTM).
- PCA & XGBoost (Principal Component Analysis & eXtreme Gradient Boosting).
- RF (Random Forest).
- RF-GB (Random Forest & Gradient Boosting).
- RF-GB-NN (Random Forest, Gradient Boosting & Neural Network).
- KNN (K-Nearest Neighbors).

- These models predict gas concentration levels based on the sensor response data.

## 4. Threshold-Based Alert Mechanism



- If the predicted gas concentration exceeds predefined safety thresholds (500 ppm for acetone and ethanol, 200 ppm for methanol), the system automatically triggers an alert.
- The alert is sent to a server, notifying users of a potentially hazardous gas level, and an alarm is activated to prompt immediate action.

This automated AI-driven approach ensures effective real-time gas monitoring, enabling rapid response to hazardous conditions and enhancing safety in industrial, medical, and environmental applications.

### Supervised learning techniques for gas classification and condition monitoring

In this study, gas detection is formulated as a classification problem to identify three gaseous chemicals: acetone, ethanol, and methanol. The classification models are developed using seven supervised learning techniques.

- Logistic Regression for Multi-Class Classification

The classification task involves multi-class classification, where a one-versus-rest (OvR) scheme is employed for logistic regression. This approach involves training separate classifiers for each gas type:

1. Acetone vs. (Ethanol & Methanol).
2. Ethanol vs. (Acetone & Methanol).
3. Methanol vs. (Acetone & Ethanol).

Additionally, logistic regression is used to classify high and low concentrations for each gas type. The model is optimized using:

- Cross-entropy loss, which measures classification performance and minimizes prediction errors.
- L2 regularization, applied to prevent overfitting by penalizing large coefficient values.
- Hybrid CNN-LSTM Model for Gas Detection

A Convolutional Neural Network (CNN) is integrated with a Long Short-Term Memory (LSTM) network in the CNN-LSTM model, capturing both spatial and temporal features in the dataset:

- The CNN layers extract spatial features from the sensor readings.
- The LSTM layers capture temporal dependencies, helping to identify time-dependent variations in gas concentrations.

To improve efficiency, Principal Component Analysis (PCA) is first applied to reduce data dimensionality in the PCA-CNN-LSTM model. The original three-dimensional dataset is reduced to two dimensions, ensuring computational efficiency without significant loss of information.

- XGBoost with Dimensionality Reduction

In the PCA-XGBoost model, Principal Component Analysis (PCA) is again used for dimensionality reduction before classification with XGBoost, reducing the number of dimensions from 3 to 2 while preserving essential features. XGBoost is optimized for structured data classification, enhancing the accuracy and speed of gas detection.

- Random Forest, Gradient Boosting, and Ensemble Models

To enhance classification accuracy, ensemble learning techniques are applied using:

- Random Forest (RF).
- Gradient Boosting (GB).
- Random Forest with Gradient Boosting (RF-GB).
- Random Forest, Gradient Boosting, and Neural Network (RF-GB-NN).

Each of these models applies supervised learning techniques to classify gas type (acetone, ethanol, or methanol) and gas condition (high or low concentration threshold). The ensemble learning approach follows a perturb-and-combine method, introducing randomization in classifier design and resulting in a diverse set of classifiers. The final ensemble prediction is derived from the average forecast of individual classifiers, improving robustness and classification accuracy.

- Linear Discriminant Analysis (LDA) for Decision Boundaries

For additional classification validation, Linear Discriminant Analysis (LDA) is implemented. LDA applies Bayes' theorem to fit conditional class densities and generates linear decision boundaries, assisting in efficient gas classification.

By employing various supervised learning techniques, the proposed AI-driven e-nose system achieves highly accurate classification and condition monitoring of gaseous chemicals. These models enable real-time, intelligent gas detection, making the system suitable for environmental monitoring, industrial safety, and IoT-based smart sensing applications.

Table 5 presents the classification accuracies of the employed machine learning models for both gas type and gas condition. The CNN-LSTM, PCA-CNN-LSTM, PCA-XGBoost, RF, RF-GB, and RF-GB-NN models all achieved perfect accuracy (1.00) for gas type classification, except for RF-GB-NN, which recorded an accuracy of 0.90.

For gas condition classification, the CNN-LSTM, PCA-CNN-LSTM, PCA-XGBoost, RF, RF-GB, and RF-GB-NN models demonstrated accuracies of 0.994, 0.9972, 0.999, 1.00, 1.00, and 1.00, respectively. However, the standalone RF model exhibited a significantly lower accuracy of 0.50. These results suggest that the progressive deep learning models significantly outperformed traditional machine learning techniques, successfully classifying both the gas type and its concentration condition with high accuracy.

To assess the reliability and accuracy of gas quantification algorithms, several key performance metrics were evaluated, each providing distinct insights into model performance.

1. Root Mean Square Error (RMS)

The RMS measures the magnitude of prediction errors, with lower RMS values indicating better model performance<sup>36</sup>:

$$RMS = \sqrt{\frac{1}{n} \sum_{i=1}^n (y_i - \hat{y}_i)^2} \tag{5}$$

where  $y_i$  represents the actual values,  $\hat{y}_i$  denotes the predicted values, and  $n$  is the total number of observations.

2. Mean Squared Error (MSE)

The MSE computes the average of the squared differences between actual and predicted values, with lower MSE values indicating a more accurate model<sup>36</sup>:

$$MSE = \frac{1}{n} \sum_{i=1}^n (y_i - \hat{y}_i)^2 \tag{6}$$

3. Mean Absolute Error (MAE)

The MAE represents the average absolute differences between actual and predicted values. A lower MAE suggests enhanced predictive performance<sup>36</sup>:

$$f(x) = \frac{1}{n} \sum_{i=1}^n (y_i - \hat{y}_i) \tag{7}$$

4. Normalized Root Mean Square Error (NRMS)

The NRMS normalizes the RMS value relative to the range of the dataset, providing a relative measure of prediction error<sup>36</sup>:

$$NRMS = \frac{RMS}{\max(y) - \min(y)} \tag{8}$$

This metric allows for comparisons across different datasets and model performances.

5. Coefficient of Determination (R<sup>2</sup>)

Accuracy	CNN-LSTM	PCA&CNN-LSTM	PCA&XGBOOST	RF	RF &gradient boost	RF-GB-NN	KNN
Gas type	1	1	1	1	1	1	0.9
Gas condition	0.994	0.9972	0.999	1	1	1	0.5

**Table 5.** Accuracies of various machine learning models for classifying Gas type and Gas condition.

The  $R^2$  value measures the proportion of variance in the dependent variable that is explained by the model. A value closer to 1 indicates a better model fit<sup>37</sup>:

$$R^2 = 1 - \frac{\sum_{i=1}^n (y_i - \hat{y}_i)^2}{\sum_{i=1}^n (y_i - \bar{y})^2} \quad (9)$$

where  $\bar{y}$  is the mean of the actual values.

## 6. Standard Deviation (SD)

The standard deviation measures the dispersion or spread of the dataset<sup>38</sup>:

$$SD = \sqrt{\frac{1}{N} \sum_{i=1}^N (X_i - \mu)^2} \quad (10)$$

where  $X_i$  represents each data point,  $\mu$  is the dataset mean, and  $N$  is the number of observations.

## 7. Limit of Detection (LOD) and Limit of Quantification (LOQ)

The LOD represents the lowest detectable quantity of a substance, while the LOQ indicates the minimum concentration that can be measured with acceptable accuracy. These metrics are critical for assessing sensor sensitivity<sup>39</sup>:

$$LOD = 3.3 \times \frac{SD}{slop} \quad (11)$$

$$LOQ = 10 \times \frac{SD}{slop} \quad (12)$$

where  $SD$  is the standard deviation of the response, and the slope represents the calibration curve slope.

The evaluation of classification accuracy and regression performance metrics demonstrates that the proposed AI-driven gas sensing models achieved exceptional classification accuracy and highly precise gas concentration estimations. The deep learning models (CNN-LSTM, PCA-CNN-LSTM, PCA-XGBoost, RF-GB, and RF-GB-NN) outperformed traditional machine learning techniques, offering enhanced reliability and robustness for real-time gas detection and quantification. These results validate the efficacy of AI-based e-nose systems in providing accurate, automated, and intelligent gas monitoring solutions.

## Performance evaluation of gas quantification algorithms

Table 6 presents the performance metrics for various gas quantification algorithms, evaluated using seven key parameters:

- Root Mean Square Error (RMS)
- Mean Squared Error (MSE)
- Mean Absolute Error (MAE)
- Normalized Root Mean Square Error (NRMS)
- Coefficient of Determination ( $R^2$ )
- Limit of Detection (LOD)
- Limit of Quantification (LOQ)

These metrics assess the models' predictive accuracy, error minimization, and sensitivity in detecting gas concentrations.

### Model performance analysis

**CNN-LSTM Model** The CNN-LSTM model demonstrated strong predictive performance, particularly for methanol, exhibiting low prediction errors and excellent  $R^2$  values. Ethanol predictions also maintained low errors and high sensitivity, while acetone predictions, though accurate, exhibited moderate errors compared to the other two gases. However, the high  $R^2$  values indicate the model's overall strong predictive capabilities.

**PCA & CNN-LSTM model** The integration of PCA with CNN-LSTM further enhanced predictive performance across all gases. Acetone and ethanol predictions were highly accurate, with minimal errors and high sensitivity. Methanol predictions, while strong, exhibited slightly higher detection and quantification limits, yet

Model	Gas Name	RMS	MSE	MAE	NRMS	R <sup>2</sup>	LOD	LOQ	SD
CNN-LSTM	Acetone	24.24	587.6	20.1	0.009973	0.998	40.626	135.422	13.5422
	Ethanol	23.65	559.38	18.241	0.0094	0.998	45.16	150.53	18.518
	Methanol	11.698	1063.23	23.33	0.01311	0.997	68.33	227.78	22.78
PCA&CNN-LSTM	Acetone	2.4516	6.01	2.054	0.0009	0.9999	4.42	13.4	1.33769
	Ethanol	0.29	0.086	0.221	0.000118	0.9999	1.23	3.72995	0.292
	Methanol	1.8	3.3	1.52	0.00073	0.9999	3.46	10.49	1.04
PCA&XGBOOST	Acetone	3.2	10.29	2.714	0.0012	0.9999	10.2	30.9	0.48452
	Ethanol	5.67	32.2	4.1	0.00229	0.9999	15.45	46.83	4.654
	Methanol	0.488	0.238	0.399	0.000197	0.9999	1.1	3.35	0.3354
RF	Acetone	0.641	0.411	0.56	0.00026	0.9999	2.1	6.389	0.6385
	Ethanol	0.6293	0.397	0.532	0.00054	0.9999	1.51	4.5778	0.4577
	Methanol	0.492	0.242	0.37	0.00019	0.9999	1.6122	4.885	0.4885
RF&GB	Acetone	$5.1 \times 10^{-13}$	$2.62 \times 10^{-25}$	$3.8 \times 10^{-13}$	$2.05 \times 10^{-16}$	1	1.12	3.394	$4.13 \times 10^{-13}$
	Ethanol	$5 \times 10^{-13}$	$2.48 \times 10^{-25}$	$4.3 \times 10^{-13}$	$2 \times 10^{-16}$	1	$1.2 \times 10^{-15}$	$3.7 \times 10^{-15}$	$4.5 \times 10^{-13}$
	Methanol	$9.1 \times 10^{-14}$	$8.25 \times 10^{-27}$	$4.6 \times 10^{-14}$	$3.65 \times 10^{-17}$	1	$2.4 \times 10^{-16}$	$7.3 \times 10^{-16}$	$9 \times 10^{-14}$
RF-GB-NN	Acetone	0.6	0.349	0.4739	0.00023	0.9999	0.00153	0.00463	0.5682
	Ethanol	0.637	0.406	0.5394	0.000255	0.9999	0.00143	0.004334	0.531
	Methanol	0.56	0.317	0.4346	0.0002	0.9999	0.0014	0.00448	0.5557

**Table 6.** Performance metrics of various Gas quantification algorithms.

remained within an acceptable range. This hybrid approach effectively improves computational efficiency while maintaining robust predictive accuracy.

**PCA & XGBoost Model** The PCA & XGBoost model also performed exceptionally well, particularly in handling methanol with very low prediction errors and high accuracy. Acetone and ethanol predictions were precise, demonstrating the effectiveness of boosting techniques combined with dimensionality reduction in gas quantification tasks.

**Random Forest (RF) Model** The RF model achieved satisfactory performance, providing low errors and high sensitivity for acetone and ethanol predictions. Methanol predictions were adequate, though detection and quantification limits were slightly higher than those observed in PCA-enhanced models. This suggests that RF alone is effective but benefits from ensemble or hybridization techniques for improved precision.

**RF & GB Model** The RF-GB model outperformed all other models, achieving near-zero errors and perfect R<sup>2</sup> values (1.00) across all gases. The model's negligible detection and quantification limits further underscore its superior sensitivity and accuracy, making it the best-performing algorithm for gas quantification.

**RF-GB-NN Model** The RF-GB-NN model exhibited performance comparable to RF-GB, providing highly accurate acetone and ethanol predictions with minimal errors. Methanol predictions were also precise, with exceptionally low detection and quantification limits, reinforcing the model's robustness and high sensitivity.

*Analysis discussion*

- Hybrid ensemble models (RF, RF-GB, and RF-GB-NN) demonstrated the highest accuracy and sensitivity, with RF-GB exhibiting the best overall performance.
- CNN-LSTM and PCA-CNN-LSTM models also performed well, particularly for methanol, confirming the effectiveness of deep learning for time-series gas detection.
- PCA & XGBoost performed strongly for all gases, validating the benefits of boosting techniques combined with dimensionality reduction.
- The choice of algorithm significantly affects quantification accuracy and sensitivity, with ensemble-based models outperforming traditional and single deep-learning approaches.
- Future research can explore the integration of additional features and advanced hybrid models to further enhance predictive accuracy and robustness in gas quantification tasks.

From the results in Table 6, the Random Forest and Gradient Boosting (RF-GB) and Random Forest and Gradient Boosting with Neural Network (RF-GB-NN) models demonstrated exceptional performance across multiple evaluation metrics. These models achieved the highest accuracy and sensitivity, making them the most suitable candidates for further analysis. The confusion matrices and actual vs. predicted gas concentration figures for these models will be examined in detail to assess their effectiveness in real-world gas quantification applications.

The integration of a Neural Network (NN) into the RF-GB model, creating the RF-GB-NN hybrid, was intended to enhance the model's ability to capture complex patterns and non-linear relationships in the dataset.

This hybrid model leverages the strengths of both ensemble methods (RF-GB) and deep learning (NN), leading to improved accuracy and generalization. The NN component contributes to:

- More precise predictions, particularly in cases with intricate data structures.
- Better generalization by reducing overfitting to the training dataset.
- Improved response sensitivity to subtle variations in gas concentration.

The RF-GB model consistently outperformed the RF-GB-NN model across key evaluation metrics, including:

- Lower error rates in Root Mean Square Error (RMS), Mean Squared Error (MSE), Mean Absolute Error (MAE), and Normalized Root Mean Square (NRMS).
- Better sensitivity, reflected in the Limit of Detection (LOD) and Limit of Quantification (LOQ) values.
- Perfect fit ( $R^2 = 1.00$ ) for RF-GB, compared to  $R^2 = 0.99$  for RF-GB-NN.

The RF-GB model's perfect  $R^2$  value (1.00) indicates that it fully explains the variance in gas concentration without any error. In contrast, the RF-GB-NN model's slightly lower  $R^2$  value (0.99), though still very high, suggests a small degree of unexplained variance.

While the Neural Network component in the RF-GB-NN model enhances non-linear feature extraction, it also introduces additional parameters and complexity. This increased complexity can:

- Increase the risk of overfitting, especially if the network is too complex relative to the dataset size.
- Slightly reduce  $R^2$  performance, as the model may fit the training data closely but struggle with generalization to unseen data.

Thus, while RF-GB-NN provides robust performance, the simpler structure of RF-GB yields optimal fitting, making it the superior model for real-world gas quantification applications.

The standard deviation (SD) values of predicted gas concentrations across different models indicate prediction stability:

- Higher standard deviations (e.g., CNN-LSTM and PCA-CNN-LSTM models) suggest greater variability, leading to less consistent predictions.
- Lower standard deviations (e.g., RF-GB and RF-GB-NN models) indicate more stable and reliable predictions, with less fluctuation.

The lower SD values of RF-GB and RF-GB-NN confirm their high reliability and consistency, making them preferable for real-time gas monitoring applications. In conclusion, the main following points are observed from the obtained results:

- RF-GB consistently outperforms RF-GB-NN, achieving perfect  $R^2$  (1.00) with lower prediction errors and better sensitivity.
- RF-GB-NN captures more complex non-linear relationships, but slight overfitting reduces its generalization capability, leading to  $R^2 = 0.99$ .
- Lower standard deviation values in RF-GB and RF-GB-NN indicate higher prediction consistency, making them ideal for stable real-time gas monitoring.
- Ensemble learning techniques (RF-GB) remain the best choice for gas quantification, while deep learning (NN) adds value in handling complex data structures but requires careful tuning to prevent overfitting.

Future research could further refine hybrid models by optimizing neural network architectures or exploring additional ensemble methods to maximize predictive performance and generalization.

Figures 18 and 19 illustrate the learning curves of the Random Forest and Gradient Boosting (RF-GB) and RF-GB-NN models, providing insights into their training performance and generalization ability for gas condition and gas type classification.

- Learning Curve Analysis for Gas Condition Classification (Fig. 18)
- RF-GB Model Performance:

The RF-GB model maintains a perfect training score of 1 across all training examples.

Its cross-validation score starts at 0.875, dips slightly to 0.825, and then rises to nearly 1 as more data is available.

This pattern suggests that as more training data is incorporated, the model improves its generalization, eventually achieving near-perfect performance.

- RF-GB-NN Model Performance:

The RF-GB-NN model's training score starts slightly below 0.99, but reaches 1 from 3000 to 5000 training examples and remains perfect thereafter.

The cross-validation score, calculated using fivefold cross-validation, begins at 0.875, decreases to 0.8 at 5000 training examples, then rises to 0.95 at 7000 examples, and approaches 1 by 9000 examples.

The slower rise in cross-validation score suggests that while RF-GB-NN initially struggles with generalization, it eventually improves as training data increases.



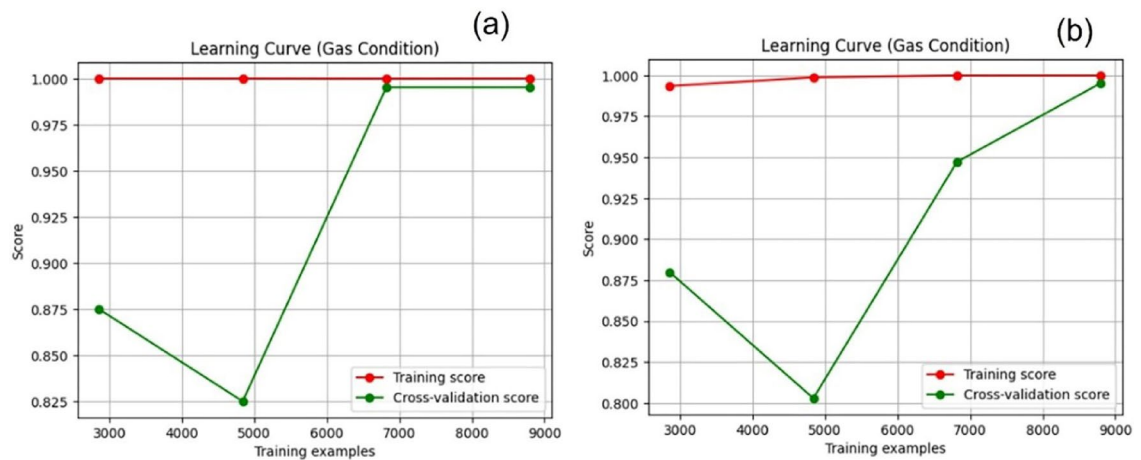


**Fig. 18.** The learning curves for the (a) RF-GB, and (b) RF-GB-NN models highlight their performance for gas conditions.

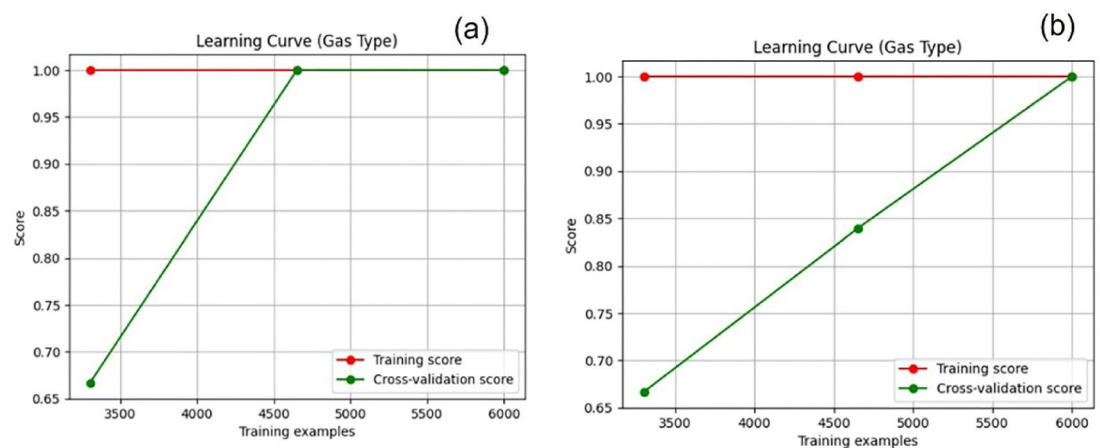


**Fig. 19.** The learning curves for the (a) RF-GB, and (b) RF-GB-NN models highlight their performance for gas type characterization.

Therefore, the RF-GB model generalizes more efficiently, reaching near-perfect validation accuracy with fewer training examples, while RF-GB-NN requires more data to stabilize its performance.

- Learning Curve Analysis for Gas Type Classification (Fig. 19)
- RF-GB Model Performance:

The RF-GB model achieves a perfect training score of 1 across all training examples.

The cross-validation score improves rapidly, increasing from 0.56 at 3300 training examples to 1 at 3600 examples.

This demonstrates fast generalization, meaning the model requires fewer samples to achieve high accuracy.

- RF-GB-NN Model Performance:

The RF-GB-NN model also achieves a perfect training score of 1 for all training examples.

However, its cross-validation score increases more gradually, starting at 0.65 at 3500 training examples and reaching 1 at 6000 examples.

This indicates that RF-GB-NN learns more slowly compared to RF-GB, requiring more training data to achieve full generalization.

Therefore, the RF-GB model outperforms RF-GB-NN in terms of rapid generalization, requiring fewer training examples to achieve perfect classification accuracy. The RF-GB-NN model improves steadily but requires significantly more data to reach optimal performance.

In conclusion, the key findings from the obtained learning curves are summarized as follows:

- RF-GB exhibits faster generalization across both gas condition and gas type classification, achieving near-perfect performance with fewer training examples.
- RF-GB-NN requires more training data to reach similar levels of accuracy, indicating a more complex learning process due to the Neural Network component.
- For gas condition classification (Fig. 18), both models ultimately achieve near-perfect accuracy, but RF-GB reaches this level more efficiently.
- For gas type classification (Fig. 19), RF-GB generalizes more rapidly, while RF-GB-NN improves gradually over a larger dataset size.
- Overall, RF-GB remains the superior model in terms of efficiency and generalization speed, while RF-GB-NN benefits from additional training data but takes longer to stabilize performance.

The performance metrics illustrated in the learning curves (Figs. 18, 19) are based on fivefold cross-validation, ensuring consistency and reliability in evaluating model performance. This cross-validation method mitigates the impact of data variability and enhances the generalization assessment of both models.

Table 7 presents a summary of the learning curves, outlining the range of training examples, training scores, and cross-validation scores for both models. This concise overview helps in understanding the learning efficiency and generalization behavior of the RF-GB and RF-GB-NN models.

In conclusion, the key findings from the obtained learning curves are summarized as follows:

- Generalization Speed for Gas Type Classification (Fig. 19):  
RF-GB exhibits faster generalization, achieving near-perfect accuracy with fewer training examples. RF-GB-NN, while still improving, requires more training data to reach similar accuracy levels.
- Fluctuations in Gas Condition Performance (Fig. 18):  
RF-GB-NN shows more pronounced fluctuations in gas condition classification, with its cross-validation score initially dropping before improving with more data. This suggests higher model sensitivity to training data volume, requiring larger datasets for stability. RF-GB, on the other hand, maintains a more stable learning trajectory, gradually improving until it reaches an optimal score.

In summary, the main observations from the results are summarized as follows:

- RF-GB is more efficient, achieving high accuracy with fewer training samples and demonstrating stable, rapid generalization.
- RF-GB-NN, while slightly more sensitive to fluctuations, ultimately benefits from additional training data, improving over time.
- For gas type classification, RF-GB outperforms RF-GB-NN in terms of speed and stability.
- For gas condition classification, RF-GB-NN requires more data to stabilize, indicating that its Neural Network component introduces additional complexity that needs larger datasets to generalize effectively.

Future work could explore hybrid optimizations, such as regularization techniques or fine-tuning the neural network architecture, to improve the RF-GB-NN model's efficiency while maintaining its ability to learn complex data patterns.

Figures 20 and 21 present the confusion matrices for the RF-GB and RF-GB-NN models, evaluating their ability to classify gas conditions (low vs. high concentration) and gas types (ethanol, methanol, acetone). These matrices provide insight into the classification accuracy and reliability of the models.

In Fig. 20, both the RF-GB and RF-GB-NN models exhibit identical 2 × 2 confusion matrices for gas condition classification, indicating perfect accuracy in distinguishing between high and low concentration levels. No misclassifications were observed, confirming that both models correctly classified all gas condition cases. This result highlights the exceptional sensitivity and reliability of the models in real-time gas monitoring applications, ensuring accurate threshold detection for hazardous gas concentrations.

Similarly, Fig. 21 displays the 3 × 3 confusion matrices for gas type classification, where both RF-GB and RF-GB-NN models achieved flawless performance. Each model successfully classified ethanol, methanol, and acetone without any errors, demonstrating their strong ability to distinguish between different gas types. This perfect classification performance indicates that both models effectively learn and differentiate the distinct patterns associated with each gas, reinforcing their suitability for precise gas identification.

Overall, the results show that both RF-GB and RF-GB-NN models deliver outstanding classification accuracy for gas condition and gas type recognition. While RF-GB achieves this high accuracy with a more efficient

Model	Characterization	Training examples	Training score	Cross-validation score
RF-GB	Gas condition	3000–9000	1.0	0.875 to nearly 1
	Gas type	3300–3600	1.0	0.56 to 1.0
RF-GB-NN	Gas condition	3000–9000	Slightly below 0.99 to 1.0	0.875 to nearly 1
	Gas type	3500–6000	1.0	0.65 to 1.0

**Table 7.** Training and cross-validation scores for RF-GB and RF-GB-NN models.

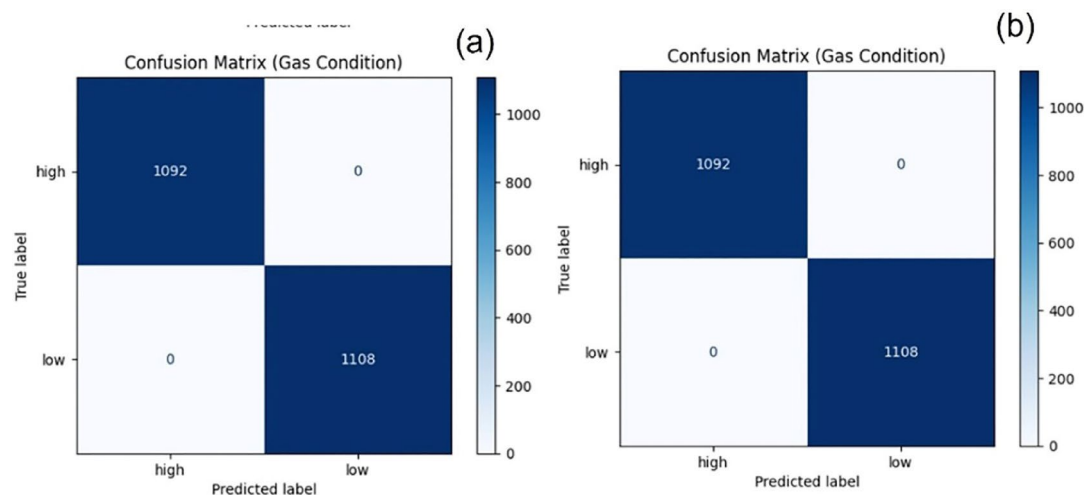


**Fig. 20.** confusion matrices for (a) RF-GB model and (b) for RF-GB-NN model for gas condition characterization.

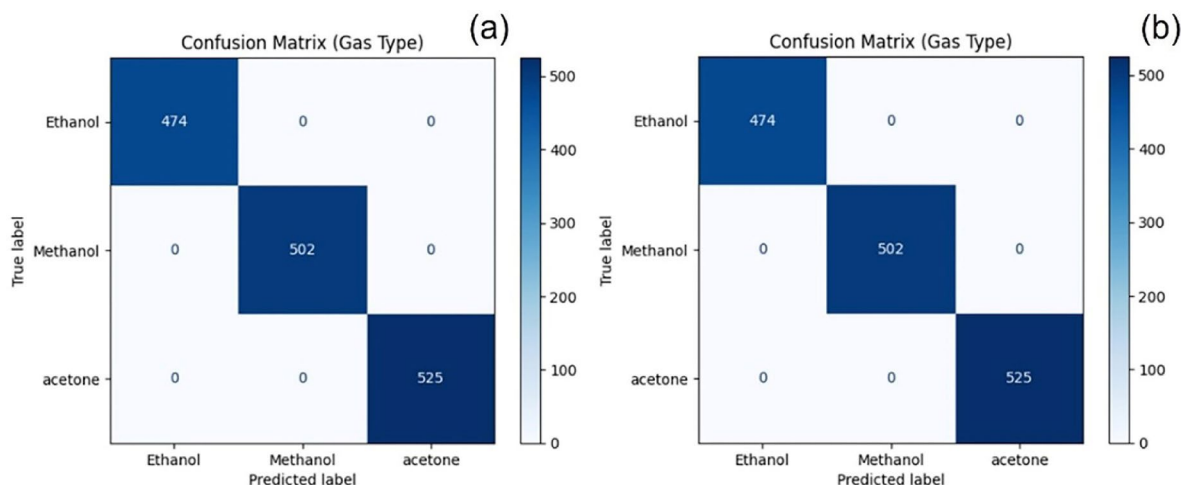


**Fig. 21.** Confusion matrices for (a) for RF-GB model and (b) for RF-GB-NN.

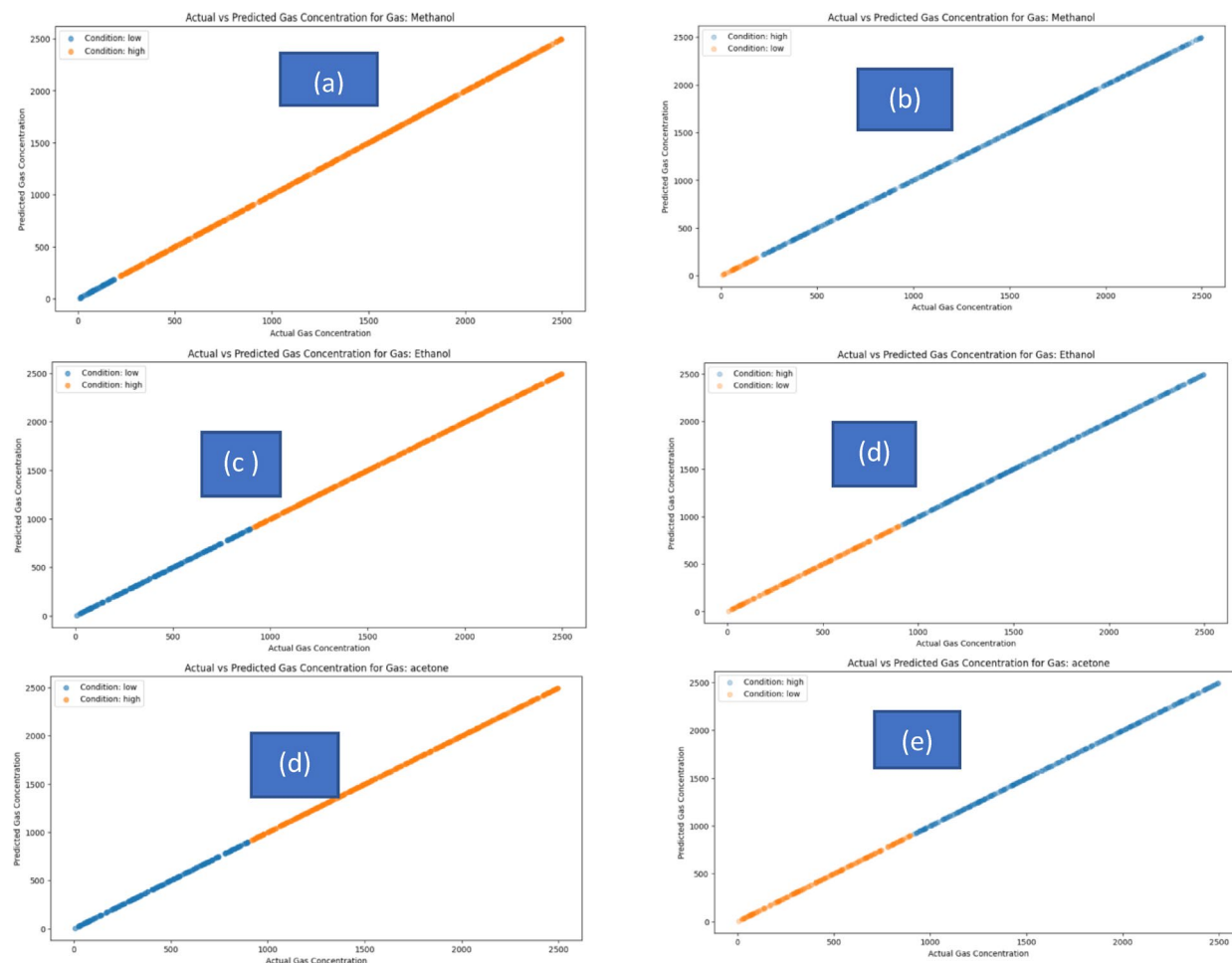
learning process, RF-GB-NN, although equally effective, requires more training data to stabilize its performance due to its increased model complexity. These findings confirm that ensemble learning techniques, particularly RF-GB, offer an optimal balance between accuracy, efficiency, and computational performance in AI-driven gas sensing systems.

Figure 22 presents the predicted versus actual gas concentration plots for the RF-GB and RF-GB-NN models, evaluating their predictive accuracy for ethanol, methanol, and acetone gases. These plots visually compare the model predictions against true gas concentrations, providing insight into their reliability across different concentration levels.

In the RF-GB model (Fig. 22a,c,e), the predicted gas concentration is represented by a blue line for low concentration cases and an orange line for high concentration cases for ethanol, methanol, and acetone, respectively. Conversely, in the RF-GB-NN model (Fig. 22b,d,f), the colors are reversed, with blue representing high concentration cases and orange representing low concentration cases.

Across all figures, the predicted versus actual gas concentration curves exhibit a strong linear trend, demonstrating a high correlation between the predicted and actual values. This linearity confirms that both models effectively generalize gas concentration levels, accurately capturing variations across different gas types and concentration ranges.

Overall, these findings reinforce the robust predictive performance of both RF-GB and RF-GB-NN models, with RF-GB maintaining a slight edge in efficiency and stability. The strong alignment between predicted and actual values underscores the models' effectiveness in real-time gas monitoring and quantification, making them suitable for high-precision AI-driven gas sensing applications.



**Fig. 22.** Predicted versus actual gas concentration for RF-GB model: (a) Ethanol gas, (c) Methanol gas, (e) Acetone gas, predicted versus gas concentration for RF-GB-NN model, (b) Ethanol, (d) Methanol, and (f) Acetone.

### In-depth discussion and analysis

This study commenced with the synthesis of hematite metal oxide nanopowders, imprinted with ethanol and methanol at varying ratios of 10%, 20%, and 25%. The synthesized nanopowders were then deposited on substrates using the spin-coating technique to fabricate gas sensors. The primary objective was to evaluate the electrical response of the sensors based on different imprinting ratios and to determine the optimal conditions for enhanced gas detection.

The analysis revealed that the ethanol-imprinted sensor (SE10, 10%) and the methanol-imprinted sensor (SM10, 10%) exhibited the highest responses, suggesting that lower imprinting ratios do not necessarily result in lower sensor responses. Notably, the ethanol-imprinted sensor exhibited the strongest response at a lower temperature of 100 °C, whereas the methanol-imprinted sensor responded best at 200 °C. These observations were recorded at a gas concentration of 100 ppm, under an absolute humidity range of 40 to 60 g/m<sup>3</sup>.

To develop an electronic nose (E-nose) system, the study integrated the three most responsive sensors:

1. Acetone-imprinted sensor at 15%, doped with palladium.
2. Ethanol-imprinted sensor at 10% (SE10).
3. Methanol-imprinted sensor at 10% (SM10).

These sensors were employed to detect acetone, ethanol, and methanol gases, generating a dataset of voltage output (Vout) versus gas concentration, ranging from 0 to 2500 ppm for each gas.

- AI model evaluation for gas detection and quantification

To analyze the dataset, seven AI models were evaluated for gas type detection and gas concentration prediction. The RF-GB (Random Forest and Gradient Boosting) and RF-GB-NN (Random Forest, Gradient Boosting, and Neural Network) models demonstrated the highest performance, achieving outstanding accuracy in both gas identification and quantification.

For gas type classification, the models' accuracy scores were 1, 1, 1, 1, 1, and 0.9, while for gas condition classification, the accuracy values were 0.994, 0.9972, 0.999, 1, 1, and 0.5, corresponding to the models CNN-LSTM, PCA&CNN-LSTM, PCA&XGBOOST, RF, RF-GB, RF-GB-NN, and KNN, respectively.

A detailed performance metric analysis (including RMS, MSE, MAE, NRMS,  $R^2$ , LOD, and LOQ) confirmed that the RF-GB model outperformed RF-GB-NN. Specifically, RF-GB exhibited lower error values (RMS, MSE, MAE, NRMS, LOD, and LOQ) and a higher  $R^2$  value of 1.00, while RF-GB-NN achieved an  $R^2$  of 0.99. These results indicate that RF-GB offers superior predictive accuracy and stability, making it the preferred model for gas quantification.

- Learning Curve Analysis of RF-GB and RF-GB-NN

The learning curve analysis provided further insights into the training and generalization capabilities of both models.

- For RF-GB:

The training score remained consistently at 1.00, indicating perfect learning from the training dataset.

The cross-validation score for gas condition classification started at 0.875 and gradually improved to nearly 1.00 as more data was introduced.

The cross-validation score for gas type classification showed a rapid increase from 0.56 to 1.00, demonstrating efficient learning and generalization.

- For RF-GB-NN:

The training score for gas type classification was consistently at 1.00, while the cross-validation score improved gradually from 0.65 to 1.00.

For gas condition classification, the training score started at 0.99, increased to 1.00, and the cross-validation score improved from 0.875 to nearly 1.00.

While RF-GB-NN required more training data to stabilize, it eventually matched RF-GB's accuracy.

- Predicted vs. Actual Gas Concentration Analysis

Graphs comparing the predicted versus actual gas concentration for ethanol, methanol, and acetone using RF-GB and RF-GB-NN displayed strong linear trends, indicating accurate predictions across all concentration levels.

- For RF-GB, the plots showed blue lines for low concentrations and orange lines for high concentrations.
- For RF-GB-NN, the color scheme was reversed, but the trend remained linear, confirming high correlation between predictions and actual gas concentrations.

These findings validate the models' robust predictive performance and their suitability for real-time gas monitoring applications.

- Conclusion and Comparative Analysis

Recent advancements in AI-driven acetone sensing have demonstrated notable progress in the field. For example,  $\alpha$ -Fe<sub>2</sub>O<sub>3</sub>-MWCNT nanocomposite sensors, combined with deep learning algorithms, have shown promising performance for exhaled breath acetone detection; however, these systems require high operating temperatures (~200 °C) and are primarily focused on biomedical applications<sup>35</sup>. Similarly, multi-input convolutional neural networks (CNNs) applied to arrays of commercial metal oxide (MOx) sensors have achieved robust classification of acetone and ethanol<sup>36</sup>. In another instance, indium-doped CeO<sub>2</sub> sensors integrated with Random Forest machine learning algorithms demonstrated enhanced acetone selectivity and rapid response but also necessitated elevated temperatures (300 °C)<sup>37</sup>. While these studies underscore the potential of AI and ML in gas detection, they are typically constrained by single-gas focus, high operational temperatures, and the absence of comprehensive electrical characterization or hybrid predictive modeling.

In contrast, the present study reveals that lower imprinting ratios (10%) of ethanol and methanol in hematite metal oxide synthesis significantly enhance sensor responses and sensitivity. Among the fabricated devices, the ethanol-imprinted sensor (SE10) exhibited an outstanding response of 92% at a low operating temperature of 100 °C. Similarly, the methanol-imprinted sensor (SM10) achieved a remarkable response of 120% at 200 °C, while the acetone-imprinted, palladium-doped sensor (Sp) demonstrated high sensitivity, recording a response of 115% at 200 °C, consistent with previous findings<sup>27</sup>. These three high-performance sensors, SE10, SM10, and Sp, were strategically integrated into the E-nose array to enable reliable and simultaneous multi-gas detection.

A key innovation of this work lies in achieving high sensitivity and selectivity at low operating temperatures, a notable advancement seldom reported in the literature. Equally novel is the first-time application and comparative evaluation of advanced hybrid machine learning models, including RF-GB, RF-GB-NN, CNN-LSTM, PCA-CNN-LSTM, PCA-XGBoost, RF, and KNN, for both quantitative and qualitative multi-gas analysis. Among these models, RF-GB and RF-GB-NN emerged as the most effective, with RF-GB delivering the lowest prediction error and highest predictive efficiency. Learning curve analyses and predicted versus actual concentration comparisons further corroborated the models' robustness and accuracy.

An additional distinguishing contribution of this study is the systematic electrical characterization of the sensor devices in diode configurations, a first in this context. The investigation revealed both ohmic and rectifying behaviors across the various molecularly imprinted samples, offering novel insights into charge



Gases detected	Materials	Models	Ref
Acetone, Ethanol, hydrogen sulfide, 2-propanol, water vapor, and benzene	Graphene functionalized with metal phthalocyanines	PCA	38
Acetone, Ethanol, Methanol	Various Metal Oxide Nanostructures	CNN, RF	39
Acetone, Ethanol	Graphene-based sensors		40
Acetone, Ethanol, Methanol	ZnO nanorods on quartz resonator	PCA	41
Acetone, Ethanol	Various MOx sensors (MQ135, TGS2600, TGS2602, MiCS6814, SGP30, BME688)	CNN	36
Water, Acetone, Ethanol	P3HT doped with triflates	PCA, LDA, kNN	42
Ethanol, Acetone	16 BME680 MOX sensors	LDA	43
NO <sub>2</sub> , acetone, ethanol, chloroform	Interdigitated Electrode (IDE)-based e-nose with Bioimpedance Spectroscopy (BIS) interface	PCA + Neural Network (multilayer, backpropagation)	44
Acetone, Ethanol, Methanol	Acetone-imprinted/Pd-doped, ethanol-imprinted, and methanol-imprinted hematite nanomaterials ( $\alpha$ -Fe <sub>2</sub> O <sub>3</sub> )	CNN-LSTM, PCA-CNN-LSTM, PCA-XGBoost, RF, RF-GB, RF-GB-NN, KNN (hybrid)	This work

**Table 8.** Summary of gases detected using different materials and models.

transport mechanisms and sensor reliability. These findings directly support enhanced 3S performance, sensitivity, selectivity, and stability, across the E-nose platform.

Collectively, these advancements establish a new benchmark for intelligent, low-temperature, multi-gas E-nose systems. The proposed framework offers a practical and scalable solution for diverse application domains, including smart home environments, industrial facilities, and healthcare monitoring.

Table 8 provides a comparative summary of different materials and AI models used in gas sensing research, demonstrating how the proposed RF-GB and RF-GB-NN approaches compare to existing methods. Thus, this study provides a comprehensive assessment of AI-driven gas detection techniques, highlighting the superiority of ensemble learning models (RF-GB and RF-GB-NN) over conventional methods. Future research could explore further optimization of hybrid models, the integration of additional gas types, and the development of real-time IoT-based gas sensing applications for enhanced environmental and industrial safety.

Conclusion and future work

This study successfully synthesized hematite metal oxide nanopowder (Fe<sub>2</sub>O<sub>3</sub>), imprinted with ethanol and methanol at varying ratios (10%, 15%, and 25%), and deposited it onto substrates using the spin coating technique for gas sensing applications. The fabricated sensors exhibited significant responses, with SE10 (ethanol-imprinted at 10%) and SM10 (methanol-imprinted at 10%) demonstrating the highest sensitivity. Notably, the ethanol-imprinted sensor (SE10) exhibited optimal response at 100 °C, whereas the methanol-imprinted sensor (SM10) showed maximum response at 200 °C. These findings indicate that increasing the imprinting ratio during synthesis does not necessarily enhance gas response, emphasizing the role of optimal imprinting conditions in sensor performance.

To implement a real-time gas sensing system, an electronic nose (E-nose) application was developed using the most reactive sensors, including the acetone-imprinted sensor at 15% doped with palladium (Sp), ethanol-imprinted sensor at 10% (SE10), and methanol-imprinted sensor at 10% (SM10). These sensors effectively detected ethanol, methanol, and acetone gases, with voltage output data collected for gas concentrations ranging from 0 to 2500 ppm. Among the seven AI models evaluated, RF-GB (Random Forest and Gradient Boosting) and RF-GB-NN (Random Forest, Gradient Boosting, and Neural Network) demonstrated superior performance in both gas identification and quantification. A detailed analysis of accuracy metrics confirmed that RF-GB slightly outperformed RF-GB-NN, exhibiting lower RMS, MSE, MAE, NRMS, LOD, and LOQ values, as well as a higher R<sup>2</sup> value, signifying better predictive accuracy and stability. The learning curve analysis provided deeper insights into the models’ training and cross-validation performance, affirming their effectiveness in characterizing gas conditions and gas types. Furthermore, predicted versus actual gas concentration graphs for ethanol, methanol, and acetone exhibited linear trends, confirming the high accuracy and reliability of both models in gas quantification tasks.

In conclusion, this study demonstrates that hematite metal oxide nanopowder imprinted with lower ethanol and methanol ratios (10%) results in superior sensor responses. The SM10 sensor achieved the highest response of 120% at 200 °C, while the SE10 sensor exhibited a response of 92% at 100 °C, underscoring the effectiveness of low imprinting ratios in enhancing gas sensitivity. The RF-GB and RF-GB-NN models proved highly effective for gas detection and quantification, with RF-GB achieving near-perfect performance (R<sup>2</sup> = 1) across all gases and extremely low RMS values of 5.1 × 10<sup>-13</sup>, 5.0 × 10<sup>-13</sup>, and 9.1 × 10<sup>-14</sup> for acetone, ethanol, and methanol, respectively. The RF-GB-NN model also demonstrated exceptional accuracy, with R<sup>2</sup> values of 0.9999 and RMS values of 0.6 for acetone, 0.637 for ethanol, and 0.56 for methanol. Beyond industrial and environmental applications, these findings highlight the potential of AI-driven gas sensing models for real-time and accurate gas monitoring, reinforcing their role in enhancing safety, environmental protection, and industrial process control. Future work may explore further optimization of AI models, integration with IoT systems, and expanding the sensor array for detecting additional gases in diverse practical applications.

While this study has demonstrated the effectiveness of hematite metal oxide nanopowder sensors and AI-driven models for gas detection and quantification, further research can explore several enhancements and optimizations. Future work could focus on expanding the sensor array to detect additional VOCs and

hazardous gases, improving the versatility of the E-nose system. Additionally, optimization of AI models through deep learning architectures or hybrid ensemble approaches could further enhance predictive accuracy and generalization. The integration of IoT-based real-time monitoring systems could also facilitate remote sensing applications in industrial safety, environmental monitoring, and healthcare. Finally, miniaturization and hardware optimization of the sensor system could enable portable and wearable gas detection devices, broadening the scope of practical implementations in smart environments and public health applications.

## Data availability

The XRD datasets generated and/or analyzed during the current study are available in the Kaggle at: <https://kaggle.com/datasets/7fb7d60b667cdf48484cb51561b678e39803184478ee419d8d9ba26996ef5f5e>.

Received: 7 March 2025; Accepted: 10 June 2025

Published online: 14 August 2025

## References

- Bajwa, J., Munir, U., Nori, A. & Williams, B. Artificial intelligence in healthcare: Transforming the practice of medicine. *Futur. Healthc. J.* **8**, e188–e194. <https://doi.org/10.7861/fhj.2021-0095> (2021).
- Morsi, I. A microcontroller based on multi sensors data fusion and artificial intelligent technique for gas identification. In *IECON 2007 - 33rd Annu. Conf. IEEE Ind. Electron. Soc.*, pp. 2203–2208 (2007). <https://doi.org/10.1109/IECON.2007.4460098>.
- Morsi, I. & Mostafa, M. M. M. Wireless gas detector system using microcontrollers, PLC and SCADA system for monitoring environmental pollution. *Appl. Mech. Mater.* **249**, 247–255 (2013).
- Li, Y. et al. Air quality forecasting with artificial intelligence techniques: A scientometric and content analysis. *Environ. Model. Softw.* **149**, 105329. <https://doi.org/10.1016/j.envsoft.2022.105329> (2022).
- Morsi, I. Discrimination of some atmospheric gases using an integrated sensor array, surface response modeling algorithms, and analysis of variance (ANOVA). In *2008 IEEE Sensors Appl. Symp.*, pp. 140–145 (2008). <https://doi.org/10.1109/SAS13374.2008.4472959>.
- Hassan, H. S., Kashyout, A. B., Morsi, I., Nasser, A. A. & Ali, I. Synthesis, characterization and fabrication of gas sensor devices using ZnO and ZnO: In nanomaterials. *Beni-Suef Univ. J. Basic Appl. Sci.* **3**, 216–221 (2014).
- Shokry Hassan, H., Kashyout, A. B., Morsi, I., Nasser, A. A. & Raafat, A. Fabrication and characterization of gas sensor micro-arrays. *Sens. Bio-Sens. Res.* **1**, 34–40. <https://doi.org/10.1016/j.sbsr.2014.04.001> (2014).
- Morsi, I. Discrimination between butane and propane in a gas mixture using semiconductor gas sensors and neural networks. In *2008 IEEE Sensors Appl. Symp.*, pp. 134–139 (2008). <https://doi.org/10.1109/SAS13374.2008.4472958>.
- Ye, Z., Liu, Y. & Li, Q. Recent progress in smart electronic nose technologies enabled with machine learning methods. *Sensors (Basel)* **21**, 7620. <https://doi.org/10.3390/s21227620> (2021).
- Van Tran, V., Park, D. & Lee, Y.-C. Indoor air pollution, related human diseases, and recent trends in the control and improvement of indoor air quality. *Int. J. Environ. Res. Public Health* **17**, 2927. <https://doi.org/10.3390/ijerph17082927> (2020).
- David, E. & Niculescu, V.-C. Volatile organic compounds (VOCs) as environmental pollutants: Occurrence and mitigation using nanomaterials. *Int. J. Environ. Res. Public Health* **18**, 13147. <https://doi.org/10.3390/ijerph182413147> (2021).
- Iman, M. Electronic noses for monitoring environmental pollution and building regression model. In *IECON Proc. (Industrial Electron. Conf.)*, pp. 1730–1735 (2008). <https://doi.org/10.1109/IECON.2008.4758215>.
- Morsi, I. Electronic nose system and artificial intelligent techniques for gases identification. *Data Storage* **80**, 175–200. <https://doi.org/10.5772/8873> (2010).
- Shetty, S. S. et al. Environmental pollutants and their effects on human health. *Heliyon* **9**(9), e19496. <https://doi.org/10.1016/j.heliyon.2023.e19496> (2023).
- Hassan, H., Kashyout, A., Moursi, I., Nasser, A. A. & Abuklill, H. Studying of gas sensing characteristics for polypyrrole coated copper nanowires. *Bothalia - A J. Bot. Life Sci.* **44**, 8 (2014).
- Fu, L., You, S., Li, G., Li, X. & Fan, Z. Application of semiconductor metal oxide in chemiresistive methane gas sensor: Recent developments and future perspectives. *Molecules* **28**, 6710. <https://doi.org/10.3390/molecules28186710> (2023).
- Rahman, N. et al. Insight into metallic oxide semiconductor (SnO<sub>2</sub>, ZnO, CuO,  $\alpha$ -Fe<sub>2</sub>O<sub>3</sub>, WO<sub>3</sub>)-carbon nitride (g-C<sub>3</sub>N<sub>4</sub>) heterojunction for gas sensing application. *Sens. Actuators A Phys.* **332**, 113128. <https://doi.org/10.1016/j.sna.2021.113128> (2021).
- Morsi, I. G., Khedr, M. E. & Aly, A. G. E. Detection of LPG gas by using multi sensors array and fabricated ZnO gas sensor. *J. Phys. Conf. Ser.* **1218**, 012005. <https://doi.org/10.1088/1742-6596/1218/1/012005> (2021).
- Busti, N. D., Parra, R. & Sousa Góes, M. Synthesis, properties, and applications of iron oxides: Versatility and challenges BT - functional properties of advanced engineering materials and biomolecules. In F.A. La Porta, C.A. Taft (Eds.), pp. 349–385 (Springer International Publishing, Cham, 2021). [https://doi.org/10.1007/978-3-030-62226-8\\_13](https://doi.org/10.1007/978-3-030-62226-8_13).
- Najaf, Z. et al. Recent trends in development of hematite ( $\alpha$ -Fe<sub>2</sub>O<sub>3</sub>) as an efficient photoanode for enhancement of photoelectrochemical hydrogen production by solar water splitting. *Int. J. Hydrogen Energy* **46**, 23334–23357. <https://doi.org/10.1016/j.ijhydene.2020.07.111> (2021).
- Abdelghani, R., Shokry Hassan, H., Morsi, I. & Kashyout, A. B. Nano-architecture of highly sensitive SnO<sub>2</sub>-based gas sensors for acetone and ammonia using molecular imprinting technique. *Sens. Actuators B Chem.* **297**, 126668. <https://doi.org/10.1016/j.snb.2019.126668> (2019).
- Khan, M. M. H., Bashir, M. T., Sikandar, M. A., Alrowais, R., Syed, S., Zahid, N., Abbas M. & Zawar, A. Green buildings and indoor air quality: A health and technological review, (2023). <https://doi.org/10.20944/preprints202308.0368.v1>.
- Amiri, V., Roshan, H., Mirzaei, A., Neri, G. & Ayesh, A. I. Nanostructured metal oxide-based acetone gas sensors: A review. *Sensors (Switzerland)* **20**, 1–25. <https://doi.org/10.3390/s20113096> (2020).
- Attallah, O. & Morsi, I. An electronic nose for identifying multiple combustible/harmful gases and their concentration levels via artificial intelligence. *Measurement* **199**, 111458. <https://doi.org/10.1016/j.measurement.2022.111458> (2022).
- National Institute for Occupational Safety and Health (NIOSH), Ethanol: Occupational Health Guideline, (2024).
- Occupational Safety and Health Administration (OSHA), Chemical Sampling Information: Methanol, (n.d.).
- Abdelghani, R. M., El-Shafai, W., Morsi, I., Taha, T. E. & Kashyout, A. E. H. B. Electrical properties of acetone imprinted hematite nanomaterials doped with Pd & Ag for gas sensing and simulation of their wireless devices. *Sens. Actuators B: Chem.* **423**, 136779. <https://doi.org/10.2139/ssrn.4905762> (2025).
- Wang, Y. et al. A general method to improve imprinting efficiency in surface protein imprinting by enhanced pre-assembly. *Acta Biomater.* **198**, 428–439. <https://doi.org/10.1016/j.actbio.2025.04.017> (2025).
- Shimizu, Y. & Egashira, M. Basic aspects and challenges of semiconductor gas sensors. *MRS Bull.* **24**, 18–24. <https://doi.org/10.1557/S0883769400052465> (1999).

30. Elyamny, S., Imam, N. I. N. G., Aquilanti, G., Cabrera, H. & Kashyout, A. Thermal transport properties for unveiling the mechanism of BiSbTe alloys in thermoelectric generation: A glance from synchrotron radiation Bi L 3 -XAFS. *J. Mater. Res. Technol.* **18**, 2261–2272 (2022).
31. Nawwar, M. A. et al. Controlling barrier height and spectral responsivity of p-i-n based GeSn photodetectors via arsenic incorporation. *RSC Adv.* **13**, 9154–9167. <https://doi.org/10.1039/d3ra00805c> (2023).
32. Che Mohamed Hussein, S., Amir, Z., Jan, B. & Khalil, M. Thermal stability analysis using iron oxide nanoparticle coated with SDS, (2022). <https://doi.org/10.21467/proceedings.141.25>.
33. Hjiri, M., Algessair, S., Dhahri, R., Mirzaei, A. & Neri, G. Gas sensing properties of hematite nanoparticles synthesized via different techniques. *RSC Adv.* **14**, 17526–17534. <https://doi.org/10.1039/d4ra02338b> (2024).
34. Rufus, A. & Philip, S. N. D. Synthesis of biogenic hematite ( $\alpha$ -Fe<sub>2</sub>O<sub>3</sub>) nanoparticles for antibacterial and nanofluid applications. *RSC Adv.* **6**, 94206–94217. <https://doi.org/10.1039/C6RA20240C> (2016).
35. Ansari, H. R., Kordrostami, Z., Mirzaei, A. & Kraft, M. Deep-learning-based blood glucose detection device using acetone exhaled breath sensing features of  $\alpha$ -Fe<sub>2</sub>O<sub>3</sub>-MWCNT nanocomposites. *ACS Appl. Mater. Interfaces* **16**, 47973–47987. <https://doi.org/10.1021/acsami.4c06855> (2024).
36. Heng, S. Y., Yap, K. Z., Lim, W. Y. & Ramakrishnan, N. AI-assisted sensor system for the acetone and ethanol detection using commercial metal oxide-based sensor arrays and convolutional neural network. *Sens. Imaging* **25**, 51. <https://doi.org/10.1007/s11220-024-00501-5> (2024).
37. Chen, X., Xing, Q., Tang, X., Cai, Y. & Zhang, M. Machine learning algorithm assisted cerium oxide based high selectivity acetone sensor. *Ceram. Int.* **50**, 41770–41779. <https://doi.org/10.1016/j.ceramint.2024.08.030> (2024).
38. Freddi, S., Marzuoli, C., Pagliara, S., Drera, G. & Sangaletti, L. Targeting biomarkers in the gas phase through a chemoresistive electronic nose based on graphene functionalized with metal phthalocyanines. *RSC Adv.* **13**, 251–263. <https://doi.org/10.1039/D2RA07607A> (2023).
39. Patil, K. V., Redekar, R. S., Bhoite, A. A., Patil, V. B., Gurav, K. V. & Tarwal, N. L. Nanostructured materials and design concept for electronic nose bt - nanostructured materials for electronic nose. In N.J. Joshi, S. Navale (Eds.), pp. 43–69 (Springer Nature Singapore, Singapore, 2024) [https://doi.org/10.1007/978-981-97-1390-5\\_3](https://doi.org/10.1007/978-981-97-1390-5_3).
40. Orzechowska, S., Mazurek, A., Świsłocka, R. & Lewandowski, W. Electronic nose: Recent developments in gas sensing and molecular mechanisms of graphene detection and other materials. *Materials (Basel)* **13**, 80. <https://doi.org/10.3390/ma13010080> (2020).
41. Ko, W., Jung, N., Lee, M., Yun, M. & Jeon, S. Electronic nose based on multipatterns of ZnO nanorods on a quartz resonator with remote electrodes. *ACS Nano* **7**, 6685–6690. <https://doi.org/10.1021/nn4027245> (2013).
42. Boujnah, A., Boubaker, A., Pecqueur, S., Lmimouni, K. & Kalbousi, A. An electronic nose using conductometric gas sensors based on P3HT doped with triflates for gas detection using computational techniques (PCA, LDA, and kNN). *J. Mater. Sci. Mater. Electron.* **33**, 1–15. <https://doi.org/10.1007/s10854-022-09376-2> (2022).
43. Palacín, J., Clotet, E. & Rubies, E. Assessing over time performance of an eNose composed of 16 single-type MOX gas sensors applied to classify two volatiles. *Chemosensors* **10**, 118. <https://doi.org/10.3390/chemosensors10030118> (2022).
44. Kaya, K. & Ebeoğlu, M. A. Development of a neural network for target gas detection in interdigitated electrode sensor-based E-nose systems. *Sensors* **24**(16), 5315. <https://doi.org/10.3390/s24165315> (2024).

## Acknowledgements

The authors would like to acknowledge the Princess Nourah bint Abdulrahman University Researchers Supporting Project number (PNURSP2025R66), Princess Nourah bint Abdulrahman University, Riyadh, Saudi Arabia. The authors would like to thank the Automated Systems and Computing Lab (ASCL) at Prince Sultan University, Riyadh, Saudi Arabia, for their support to this work. In addition, the authors wish to acknowledge the editor and anonymous reviewers for their insightful comments, which have improved the quality of this publication.

## Author contributions

All authors reviewed the manuscript. All authors are equally contributed.

## Funding

This work is supported by Princess Nourah bint Abdulrahman University Researchers Supporting Project number (PNURSP2025R66), Princess Nourah bint Abdulrahman University, Riyadh, Saudi Arabia.

## Declarations

## Competing interest

The authors declare no competing interests.

## Ethical approval

All authors are contributing and accepting to submit the current work.

## Consent to participate

All authors are contributing and accepting to submit the current work.

## Consent to publish

All authors agree to submit and publish the submitted work.

## Additional information

**Correspondence** and requests for materials should be addressed to W.E.-S.

**Reprints and permissions information** is available at [www.nature.com/reprints](http://www.nature.com/reprints).

**Publisher's note** Springer Nature remains neutral with regard to jurisdictional claims in published maps and institutional affiliations.

**Open Access** This article is licensed under a Creative Commons Attribution-NonCommercial-NoDerivatives 4.0 International License, which permits any non-commercial use, sharing, distribution and reproduction in any medium or format, as long as you give appropriate credit to the original author(s) and the source, provide a link to the Creative Commons licence, and indicate if you modified the licensed material. You do not have permission under this licence to share adapted material derived from this article or parts of it. The images or other third party material in this article are included in the article's Creative Commons licence, unless indicated otherwise in a credit line to the material. If material is not included in the article's Creative Commons licence and your intended use is not permitted by statutory regulation or exceeds the permitted use, you will need to obtain permission directly from the copyright holder. To view a copy of this licence, visit <http://creativecommons.org/licenses/by-nc-nd/4.0/>.

© The Author(s) 2025